Physics of a clumpy lensed galaxy at z=1.6

M. Girard[1], M. Dessauges-Zavadsky[1], D. Schaerer[1,2], J. Richard[3], K. Nakajima[4,5], and A. Cava[1]

[1] Observatoire de Genève, Université de Genève, 51 Ch. des Maillettes, 1290 Sauverny, Switzerland
  e-mail: marianne.girard@unige.ch
[2] CNRS, IRAP, 14 Avenue E. Belin, 31400 Toulouse, France
[3] Univ Lyon, Univ Lyon1, Ens de Lyon, CNRS, Centre de Recherche Astrophysique de Lyon UMR5574, F-69230, Saint-Genis-Laval, France
[4] European Southern Observatory, Karl-Schwarzschildstasse 2, 85748 Garching, Germany
[5] National Astronomical Observatory of Japan, 2-21-1 Osawa, Mitaka, Tokyo 181-8588, Japan

ABSTRACT

Observations have shown that massive star-forming clumps are present in the internal structure of high-redshift galaxies. One way to study these clumps in detail with a higher spatial resolution is by exploiting the power of strong gravitational lensing which stretches images on the sky. In this work, we present an analysis of the clumpy galaxy A68-HLS115 at $z = 1.5858$, located behind the cluster Abell 68, but strongly lensed by a cluster galaxy member. Resolved observations with SINFONI/VLT in the near-infrared (NIR) show Hα, Hβ, [NII], and [OIII] emission lines. Combined with images covering the B band to the far-infrared (FIR) and CO(2-1) observations, this makes this galaxy one of the only sources for which such multi-band observations are available and for which it is possible to study the properties of resolved star-forming clumps and to perform a detailed analysis of the integrated properties, kinematics, and metallicity. We obtain a stability of $v_{rot}/\sigma_0 = 2.73$ by modeling the kinematics, which means that the galaxy is dominated by rotation, but this ratio also indicates that the disk is marginally stable. We find a high intrinsic velocity dispersion of 80 ± 10 km s^{-1} that could be explained by the high gas fraction of $f_{gas} = 0.75 \pm 0.15$ observed in this galaxy. This high f_{gas} and the observed sSFR of 3.12 Gyr^{-1} suggest that the disk turbulence and instabilities are mostly regulated by incoming gas (available gas reservoir for star formation). The direct measure of the Toomre stability criterion of $Q_{crit} = 0.70$ could also indicate the presence of a quasi-stable thick disk. Finally, we identify three clumps in the Hα map which have similar velocity dispersions, metallicities, and seem to be embedded in the rotating disk. These three clumps contribute together to $\sim 40\%$ on the SFR$_{H\alpha}$ of the galaxy and show a star formation rate density about ~ 100 times higher than HII regions in the local Universe.

Key words. galaxies: high redshift – galaxies: kinematics and dynamics

1. Introduction

Clumpy galaxies have been observed for the first time between redshift 0.5 and 3 by Cowie et al. (1995) using Hubble Space Telescope (HST) high-resolution imaging. More recent observations using deep imaging, for example in the Hubble Ultra Deep Field, have confirmed the presence of these star-forming clumps in the internal structure of the galaxy disks (e.g. Elmegreen et al. 2007, 2009; Livermore et al. 2012). Integral field unit (IFU) observations have also played an important role in our understanding of these clumps and their host galaxies by providing key information about their kinematics and physical properties (e.g. Förster Schreiber et al. 2009, 2011; Genzel et al. 2011; Wisnioski et al. 2012; Livermore et al. 2015).

The size of these clumps has been reported to range from a few dozen parsecs to a few kiloparsecs from observations at $z = 1-2$ (e.g. Livermore et al. 2012; Swinbank et al. 2012; Livermore et al. 2015; Cava et al. 2018), whereas the mass lies around $10^{8-9} M_\odot$ (e.g. Förster Schreiber et al. 2011; Guo et al. 2012). However, it has been shown recently by Dessauges-Zavadsky et al. (2017) that the masses of these clumps are probably significantly lower, by one or more orders of magnitude ($\sim 10^7$ M$_\odot$). Indeed, a limited spatial resolution could cause an increase of the mass obtained due to the clustering of clumps of smaller masses, and, more importantly, the sensitivity limit impacts the clump masses even more strongly by inducing a bias against the

low-mass clumps (Dessauges-Zavadsky et al. 2017; Tamburello et al. 2017; Cava et al. 2018).

The properties of these massive clumps differ from what we observe in local HII regions. Using Hα observations, Jones et al. (2010) find that the star formation rate (SFR) density can reach 100 times higher values for clumps at $z = 1.7 - 3.1$. From CO observations, Cañameras et al. (2017) find SFR densities up to 2000 M$_\odot$ yr^{-1} kpc^{-2} for clumps of a massive galaxy at $z = 1.5$, which is in the range of maximal starbursts. Their formation is also probably due to internal processes in the galaxy disk instead of mergers. Merging systems rather than internal gravitational instabilities would result in disturbing the dynamics of the disk, while the observations and simulations often show clumps which are embedded in a rotating disk (e.g. Förster Schreiber et al. 2011; Bournaud et al. 2014; Tamburello et al. 2015; Livermore et al. 2015; Mandelker et al. 2017; Cava et al. 2018). It is believed that these clumps are formed through fragmentation processes of unstable disks (Dekel et al. 2009).

To better understand the nature of these clumps and the role they play in the galaxy evolution, several studies have established different scaling relations using the clump properties. It has been found that their surface brightness is evolving with redshift, which could be explained by the higher gas fraction observed in high-redshift galaxies and the fragmentation on larger scales in these systems (Livermore et al. 2012, 2015). By com-
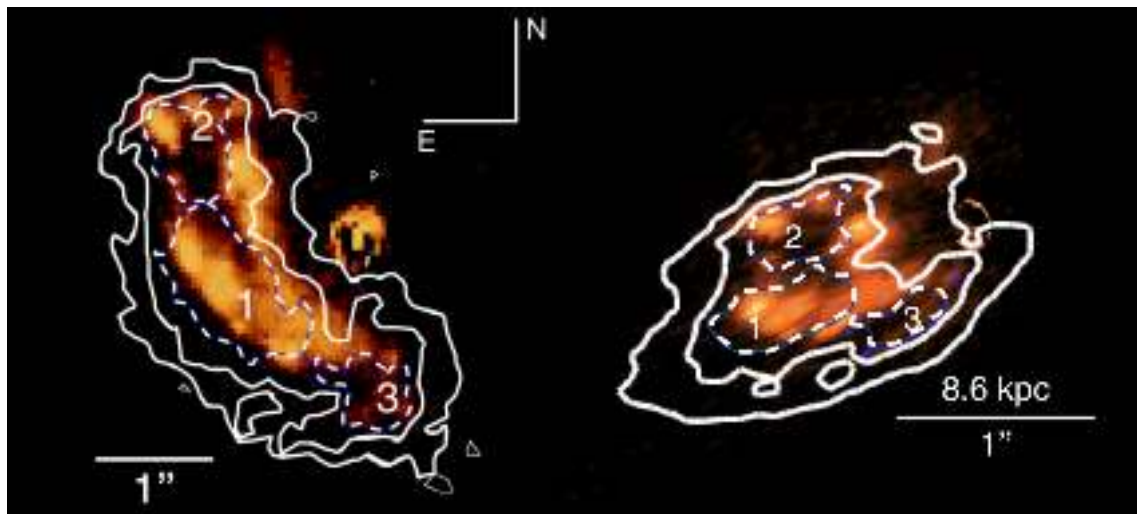
Fig. 1: HST/F814W images of A68-HLS115 in the image (left panel) and source plane after reconstruction (right panel). White dashed contours represent the Hα clumps and the white solid contours the Hα surface brightness measured in the image (left panel) and source plane (right panel) surface brightness maps corresponding to 0.64 and 1.28 $\times 10^{-16}$ erg s^{-1} cm^{-2} arcsec^{-2}. The surface brightness is conserved between the image and source plane. The cluster galaxy which is acting as a lens has been removed from the two images.

paring the clump properties to the properties of the host galaxies, Livermore et al. (2012) find a scaling relation between the clump surface brightness and the surface density of the host galaxy, meaning that the properties of these clumps are strongly related to the host galaxy. Also, Dessauges-Zavadsky et al. (2017) have shown that the maximum clump mass is correlated to the host mass.

Nevertheless, smaller clumps are often not resolved by direct observations and it is then impossible to study their physical properties. One way to study these clumps in detail with a better spatial resolution is by using strong gravitational lensing which stretches images on the sky (e.g. Jones et al. 2010; Swinbank et al. 2011; Livermore et al. 2012; Wuyts et al. 2012; Adamo et al. 2013; Livermore et al. 2015; Dessauges-Zavadsky et al. 2017; Cava et al. 2018; Patrício et al. 2018). In addition to a better spatial resolution, the magnification effect caused by the lens allows to one obtain a better signal-to-noise ratio (S/N) than direct observations for a galaxy with the same luminosity.

Gravitational lensing can also provide more information about the kinematics and metallicity of galaxies and can allow to reach a lower stellar mass range of galaxies more difficult to observe with direct observations (e.g. Jones et al. 2010; Livermore et al. 2015; Leethochawalit et al. 2016; Mason et al. 2017; Girard et al. 2018; Patrício et al. 2018). Leethochawalit et al. (2016) point out that a high spatial resolution can reveal much more complex kinematics and metallicity gradient. Their work, which uses strong gravitational lensing and studies low-mass galaxies ($\log(M_\star/M_\odot) \sim 9.5$) at $z \sim 2$, does not agree with a simple rotation disk model most of the time. They obtain a fraction of only 36% rotation-dominated galaxies in their sample.

In this work, we present an analysis of the galaxy A68-HLS115 at $z = 1.5858$, located behind the galaxy cluster Abell 68, but strongly lensed by a cluster galaxy member. A detailed study of the integrated physical properties of this galaxy has already been performed, exploiting the detection of this galaxy

through the B band up to the far-infrared (FIR) band[1] (Sklias et al. 2014) and in CO(2-1) observations with the IRAM interferometer at the Plateau de Bure, France (Dessauges-Zavadsky et al. 2015).

By combining our IFU observations obtained with SIN-FONI/VLT to these previous studies, this makes this galaxy one of the only sources for which such multi-band observations are available and for which it is possible to study the properties of resolved star-forming clumps and to perform at the same time a detailed analysis of the galaxy metallicity and kinematics. This source is also one of the most gas-rich galaxies (with a molecular gas fraction of 75%) known at redshifts higher than one.

The paper is organized as follows. Section 2 describes the results of previous studies of the galaxy A68-HLS115 which have been done by our group (Sklias et al. 2014; Dessauges-Zavadsky et al. 2015). In Sect. 3, we present SINFONI/VLT observations and data reduction. In Sect. 4, we explain the lens modeling and measurements of the emission lines. Section 5 presents our result on the integrated physical properties, metallicity, kinematics, and properties of clumps of the galaxy. We finally present our conclusions in Sect. 6.

In this paper, we use a cosmology with : $H_0 = 70$ km s^{-1} Mpc^{-1}, $\Omega_M = 0.3$, and $\Omega_\Lambda = 0.7$. When using values calculated with the initial mass function (IMF) of Salpeter (1955), we correct by a factor 1.7 to convert to a Chabrier (2003) IMF.

2. The galaxy A68-HLS115

Sklias et al. (2014) have derived several physical properties of A68-HLS115 from the spectral energy distribution (SED), such as the infrared (IR) luminosity integrated from 8 μm to 1000 μm, the dust temperature, T_{dust}, the ultraviolet (UV) luminos-

---

[1] B band from CFHT/12k, F702W and F814W from HST, z band from FORS3/VLT, J and H bands from ISAAC, Ks photometry from UKIRT, 3.6 μm and 4.5 μm from Spitzer/IRAC, 24 μm from MIPS, 100 μm and 160 μm from Herschel/PACS, and 250 μm, 350 μm and 500 μm from Herschel/SPIRE
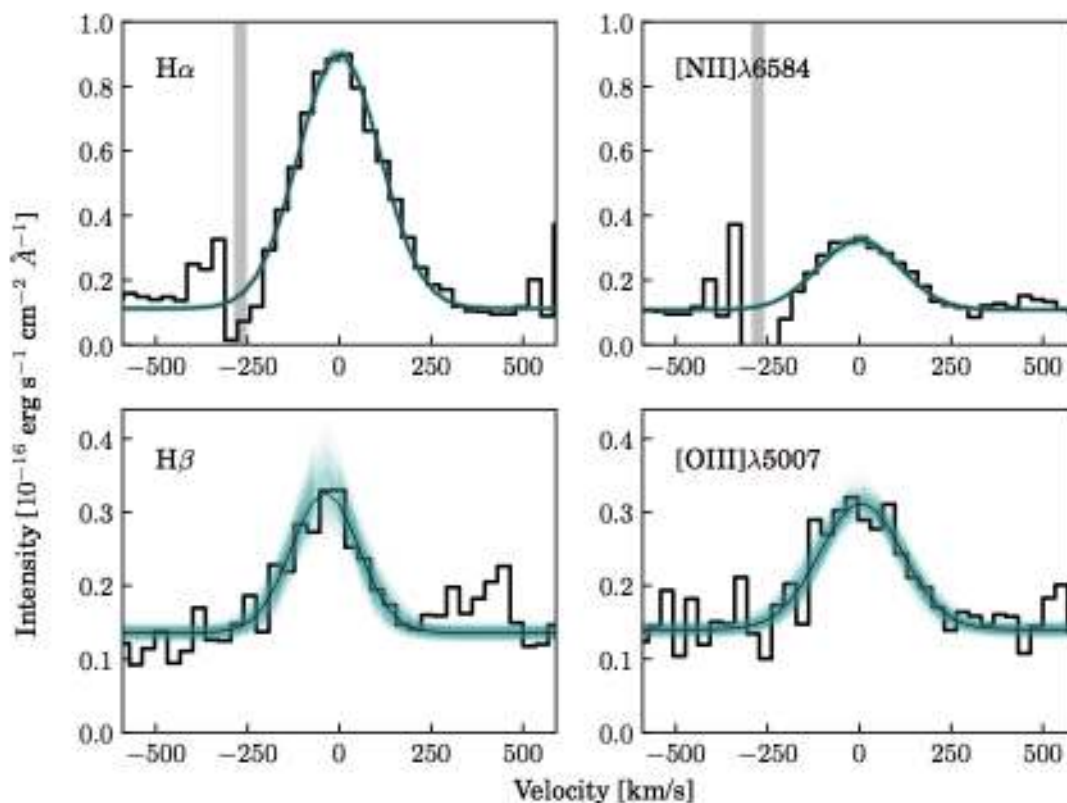
Fig. 2: Integrated Hα, Hβ, [NII] and [OIII] emission lines from the SINFONI/VLT data in the image plane. The zero velocity corresponds to the center of the Hα emission line. The 1000 realizations obtained with the Monte Carlo simulation are shown in blue and the best fit is shown in black. The gray lines show the positions of skylines.

Table 1: Physical properties of A68-HLS115 from Sklias et al. (2014) and Dessauges-Zavadsky et al. (2015).

Parameters	Values
L_{IR} [10^{12} $L_\odot$]	1.12 ± 0.06
L_{UV} [10^{10} $L_\odot$]	2.17 ± 0.20
$M_\star$ [10^{10} $M_\odot$]	$2.63^{+0.54}_{-0.65}$
SFR_{SED} [$M_\odot yr^{-1}$]	$81.4^{+8.5}_{-19}$
SFR(IR+UV) [$M_\odot yr^{-1}$]	118 ± 6
sSFR= $SFR_{SED}/M_\star$ [Gyr^{-1}]	3.12
$A_{V\,IR/UV}$[a]	$1.58^{+0.30}_{-0.10}$
T_{dust} [K]	37.5 ± 1
z_{CO}	1.5859
F_{CO}[b] [Jy km s^{-1}]	2.00 ± 0.30
M_{gas}[c] [$10^{10} M_\odot$]	7.83
f_{gas}	0.75 ± 0.15

Notes. The values have been adjusted to the Chabrier IMF and corrected for a lensing magnification of $\mu = 4.6$ (see Sect. 4.1). [a] A_V is obtained from the ratio of L_{IR} over L_{UV} as discussed in Sklias et al. (2014) and Schaerer et al. (2013). [b] Observed CO(2-1) line integrated flux. [c] M_{gas} is obtained assuming a CO-to-H$_2$ conversion factor of 4.36 $M_\odot/$K km s^{-1} pc^2.

ity, L_{UV}, the stellar mass, $M_\star$, the SFR, the specific star forma-tion rate, sSFR, and the extinction, A_V. We present these quantities in Table 1. Overall, the analysis reveals a young galaxy of ~ 130 Myr still actively producing new stars since a recent starburst took place. This galaxy of $M_\star = 2.63^{+0.54}_{-0.65} \times 10^{10}$ M$_\odot$ and $SFR_{SED} = 81.4^{+8.5}_{-19}$ M$_\odot yr^{-1}$ also lies above the main sequence (MS), computed at the same redshift and stellar mass, with an offset of 0.3 dex, placing it within the accepted thickness of the MS, $0.3 < sSFR/sSFR_{MS} < 3$ (e.g., Daddi et al. 2007; Rodighiero et al. 2010; Salmi et al. 2012). Figure 1 shows the HST/F814W images in the image and source plane after the reconstruction.

The integrated CO emission properties of A68-HLS115, that is, redshift, observed CO(2-1) flux, molecular gas mass, M_{gas}, and molecular gas fraction, f_{gas}, from Dessauges-Zavadsky et al. (2015) are also listed in Table 1. The CO emission analysis shows a very high gas fraction ($f_{gas} = 0.75 \pm 0.15$), making this galaxy one of the most gas-rich known for a redshift larger than one.

In this work, we use a total magnification factor of $\mu = 4.6 \pm 0.4$. This value is different from the one used in Sklias et al. (2014) and Dessauges-Zavadsky et al. (2015) since we did further adjustments to improve the gravitational lens model (see Sect. 4.1). All the physical parameters from Sklias et al. (2014) and Dessauges-Zavadsky et al. (2015) presented in this work have been corrected for this new magnification.

Table 2: Integrated and kinematic properties.

Parameters	Values
Redshift	1.58582 ± 0.00005
Total magnification	4.6 ± 0.4
SFR$_{H\alpha}{}^{a}$ [M$_\odot$yr^{-1}]	202 ± 51
$A_{V\,H\alpha/H\beta}$	2.90 ± 0.58
$A_{V\,IR/UV}/A_{V\,H\alpha/H\beta}$	0.54
$12+\log(O/H)_{N2}$	8.58 ± 0.07
$12+\log(O/H)_{O3N2}$	8.52 ± 0.10
$\sigma_{\rm int}$ [kms^{-1}]	109 ± 3
σ_0 [km s^{-1}]	80.5 ± 10
$v_{\rm rot}$ [km s^{-1}]	218^{+12}_{-31}
$v_{\rm rot}/\sigma_0$	2.73
PA^{b} [°]	-25 ± 7
i [°]	48 ± 15

Notes. $^{(a)}$ The SFR has been corrected for lensing and dust attenuation . $^{(b)}$ The position angle, PA, is defined as 0° for the north (up) and 90° for the East (left).

3. Observations and data reduction

The near-infrared (NIR) IFU observations were undertaken with SINFONI on VLT in service mode (ID: 092.B-0677(A), PI; Zamojski) on October Oct 6–8, 2013. SINFONI was used in the seeing limited mode, and adopted the $8'' \times 8''$ field of view of the widest 0.25′ scale. SINFONI IFU was taken using the J- and H-band filters sampling the wavelength ranges of 1.1–1.4 and 1.45–1.85 μm with the resolving power of $R \sim 2000$ and ~ 3000, respectively. Individual exposures of 300 s were taken in both J- and H-band. We adopted two ABBA dithering patterns of eight exposures per OB to perform sky subtraction with two positions, while keeping the galaxy within the field-of-view of the instrument. The seeing during the observations was $\sim 0.6''$–0.8″. Two OBs in J-band and two in H-band resulted in a total on-source integration time of 1.3 hours in each band.

The SINFONI data was reduced using recipes in the standard ESO SINFONI pipeline (v.2.5.2) operated through esoreflex (v.2.8). The pipeline corrected for sky background, flat field, and distortions, and spectrally calibrated each individual slice before reconstructing a 3D data cube for each individual exposure data. We additionally performed a sky background subtraction for an A-position image by subtracting an average B-position image created from the previous and following images, both of which were optimally scaled. This was feasible because the dither size was significantly larger than our science source size. We aligned individual cubes in the spatial direction and made a composite by averaging them with a 2σ-clipping rejection. Flux solutions and telluric absorption correction were obtained from B8- and B9-type bright stars ($K_{\rm Vega} = 7.2$–7.5) observed at similar times and airmasses. The intrinsic spectra of the stars were removed by dividing the observed stellar spectrum by the templates created by a stellar spectral synthesis program (SPECTRUM; Gray & Corbally 1994) based on the Kurucz (1993)'s atmosphere models. We finally registered the processed J- and H-band cubes to the astrometry of the HST/F814W image by using the several bright objects commonly detected in the F814 image and SINFONI 2D images, which were created from the 3D cubes collapsed in the wavelength direction.

4. Analysis

4.1. Gravitational lens modeling

We look into modelling the lensing effects of A68-HLS115 to reconstruct its intrinsic morphology. This galaxy is lensed by the combination of the cluster Abell 68 on a large scale, at a distance of 42 arcsec from the BCG, as well as the very near cluster member (residuals seen in Fig.1). We use the well-constrained mass model of Abell 68 which was presented in detail in Richard et al. (2007) and later improved in Richard et al. (2010). Following the scaling relations found for cluster members, this model predicts a velocity dispersion of ~150 km s^{-1} for the cluster member affecting HLS115, based on its luminosity. However, for such a mass the emission peaks seen in continuum and Hα images (Fig.1) would have symmetric pairs which are not detected in the images. We use the curvature of the emission in A68-HLS115 and the lack of multiple images to constrain this velocity dispersion to 80 km s^{-1}, as a lower value would make the reconstructed source highly elongated. Our model is consistent with the presence of a low-surface-brightness Einstein radius surrounding the lensing galaxy, as seen in the Hα map in the image plane. Because of the uncertainty in the velocity dispersion, we derive a total magnification factor of $\mu = 4.6 \pm 0.4$ for A68-HLS115 and the derived parameters (such as the physical scales) have a typical uncertainty of 10%. This magnification factor is different from the one used in Sklias et al. (2014) and Dessauges-Zavadsky et al. (2015) of $\mu \sim 15$ since they mostly used the original model from Richard et al. (2007) without any adjustment.

4.2. Emission line measurement

The Hα, Hβ, [NII]$\lambda6584$, and [OIII]$\lambda5007$ emission lines are detected in the integrated spectrum and the main emission lines obtained in the image plane are presented in Fig. 2. Each emission line is fitted individually following a Gaussian model and using a χ^2 minimization (Levenberg-Marquardt algorithm), except [NII]$\lambda6584$ for which we impose the same full-width at half maximum (FWHM) and relative velocity as the Hα line since one side of the [NII]$\lambda6584$ emission line is strongly affected by a skyline. All pixels affected by the skylines are masked during the fitting process. To determine the uncertainties, we perform Monte Carlo simulations perturbing the flux of every pixel with an error defined as the standard deviation of the continuum around the emission line and fitting 1000 realizations per emission line as shown in blue in Fig. 2. As a result, we obtain an accurate redshift, the flux, and the FWHM of each emission line and their associated uncertainties. We find observed fluxes of 12.45 ± 0.22, 1.83 ± 0.23, 3.43 ± 0.16, and 2.10 ± 0.32 in units of 10^{-16} erg s^{-1} cm^{-2} for Hα, Hβ, [NII]$\lambda6584$, and [OIII]$\lambda5007$, respectively.

To determine the Hα luminosity, we first correct the Hα flux for the foreground dust attenuation caused by the Galaxy (using the value from the NASA/IPAC Extragalactic Database). We then correct for the dust attenuation in the galaxy itself with the Balmer decrement (Hα/Hβ) and the relation from Calzetti et al. (2000). We use a $R_V = 4.05$ and derive the star formation rate, SFR$_{H\alpha}$, following the Kennicutt (1998) equation:

$$\mathrm{SFR}_{H\alpha} = 7.9 \times 10^{-42}\, L(H\alpha) \times \frac{1}{1.7} \times \frac{1}{\mu}, \qquad (1)$$

where the factor 1.7 is the correction for the Chabrier (2003) IMF, and μ is the magnification. As a result, we obtain a lensing-corrected value of SFR$_{H\alpha} = 202 \pm 51$ M$_\odot$ yr^{-1}. The main source of

uncertainty of SFR$_{H\alpha}$ is due to the extinction correction, which is high (see Sect. 5.1).

We derive the integrated velocity dispersion, σ_{int}, from the FWHM ($\sigma_{obs} = c/\lambda_{obs} \times$ FWHM/2.355, where c is the light speed and λ_{obs} is the wavelength of the observed line) and by correcting the observed velocity dispersion, σ_{obs}, for the instrumental broadening, σ_{instr}, which is obtained from the skylines:

$$\sigma_{int} = \sqrt{\sigma_{obs}^2 - \sigma_{instr}^2}. \qquad (2)$$

We get a value of $\sigma_{int} = 109 \pm 3$ km s^{-1} from the Hα emission line.

We are also able to perform Gaussian fits, in the same way as the integrated spectrum, on the Hα and [NII]λ6584 emission lines in individual spaxels in the image plane to obtain the flux, the [NII]/Hα ratio, velocity, and velocity dispersion maps. We reject the spaxels where the S/N is lower than three. The Hβ and [OIII]λ5008 emission lines are too faint in individual spaxels. We used the Lenstool best model to reconstruct the measured maps (Hα flux, the [NII]/Hα ratio, S/N, and kinematics) into a regular grid in the source plane, fixing the source plane spaxel grid to one fifth of the image plane SINFONI spaxels to follow the magnification factor along the shear direction (see Figs.6 and Fig. 4, respectively). This way we kept a similar sampling of the point spread function (PSF) to the image plane in the direction of the best resolution.

5. Physical properties

5.1. Star formation rate and attenuation comparisons

We now analyze the Hα derived star formation rate and the different measures of the attenuation we obtain from the integrated spectrum of A68-HLS115. The main integrated properties are summarized in Table 2. The redshift determined with the Hα emission line of $z = 1.58582 \pm 0.00005$ is in good agreement with the redshift found with the CO emission (see Table 1).

In A68-HLS115, we are able to measure both the SFR$_{H\alpha}$ corrected from the dust attenuation using the Balmer decrement (Hα/Hβ ratio) and the SFR(IR+UV) derived from the UV and IR luminosities. We find that SFR$_{H\alpha}$ is ~ 1.7 times larger than SFR(IR+UV) when carefully taking into account the differential amplification effects by measuring the Hα flux in the source plane.

Given the relatively large uncertainty on the extinction correction from the Balmer decrement, the SFR$_{H\alpha}$ agrees, however, within $\sim 1.5\sigma$ with SFR(IR+UV). Relatively few star-forming galaxies at $z \gtrsim 1$ have joint measurements of the Balmer decrement, SFR$_{H\alpha}$, and the UV+IR coverage to determine SFR(IR+UV) (see e.g. Price et al. 2014; Shivaei et al. 2016; Puglisi et al. 2017). Studying 12 $z \sim 1.6$ starburst galaxies with SFR(IR) $\sim 200 - 400$ M$_\odot$ yr^{-1}, approximately eight times above the main sequence, Puglisi et al. (2017) find that the extinction-corrected SFR$_{H\alpha}$ traces only a small fraction of the total SFR, comparable to cases of local ultraluminous infrared galaxies (ULIRGs). Examining somewhat less extreme galaxies at $z \sim 2$, Shivaei et al. (2016) find good agreement between Balmer-decrement-corrected SFR$_{H\alpha}$ and the total SFR(IR+UV). In our case, A68-HLS115 is a galaxy selected for its Herschel detection (Sklias et al. 2014), with properties similar to those of Shivaei et al. (2016). Although we find that SFR$_{H\alpha}$ > SFR(IR+UV), this is not incompatible (within the uncertainties) with the results of Shivaei et al. (2016), and the discrepancy is
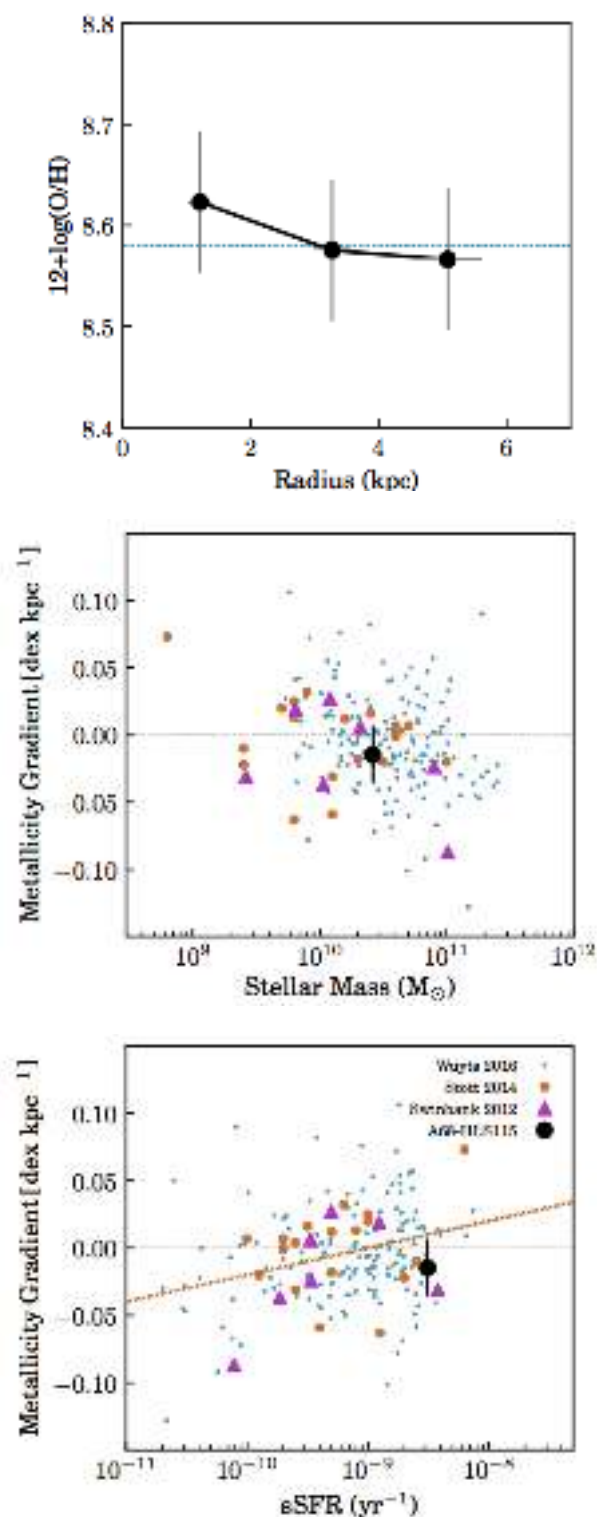

Fig. 3: Oxygen abundance as a function of the radius derived from Pettini & Pagel (2004) N2 indicator (top panel), metallicity gradient as a function of stellar mass (middle panel), and metallicity gradient as a function of sSFR (bottom panel). The blue line represents the oxygen abundance derived from the integrated spectrum. The gray lines indicate a value for the metallicity gradient of zero and the orange line is the relation obtained by Stott et al. (2014) from the combination of their data, Rupke et al. (2010), Swinbank et al. (2012), and Queyrel et al. (2012). We include the samples of Swinbank et al. (2012), Stott et al. (2014), and Wuyts et al. (2016) for comparison.
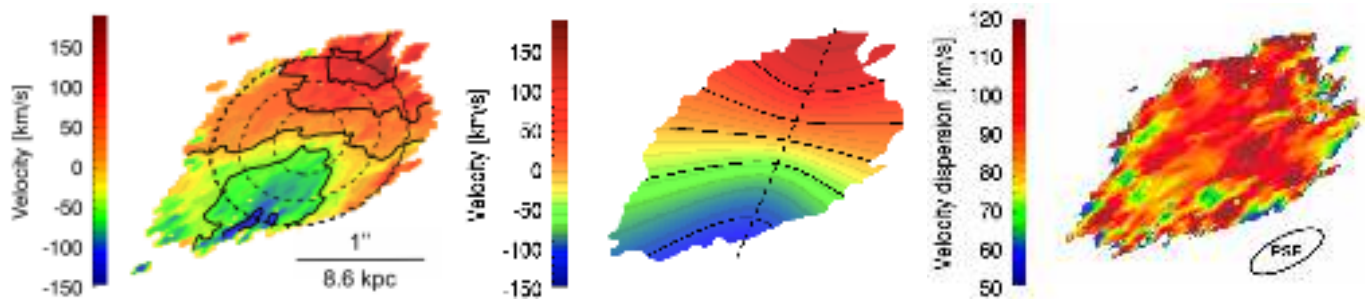
Fig. 4: Observed velocity (left panel), velocity from the model (middle panel), and velocity dispersion (right panel) in the source plane. Black lines in the velocity maps represent velocities of -100, -50, 0, 50 and 100 km s^{-1}. The black dashed ellipses (left panel) show the three annuli obtained using the Krajnović et al. (2006) method to derive the metallicity gradient. The black dashed line (middle panel) represents the major axis.
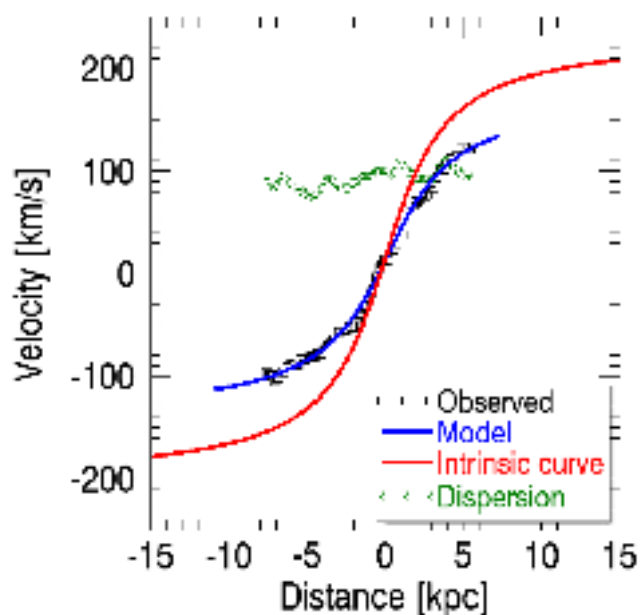

Fig. 5: Rotation curve extracted on the major axis of the velocity maps. The black squares and the blue line represent the curve extracted from the observed velocity map and velocity map from the model, respectively. The red line shows the intrinsic rotation curve from the model, corrected for inclination. The green diamonds represent the velocity dispersion profile.

negligible if Hα is extinction-corrected with the Galactic law from Cardelli et al. (1989), as pointed out by Reddy et al. (2015).

The measure of the Balmer-decrement and the IR and UV luminosities of our source allow us to determine the attenuation of the ionized gas and the stellar continuum, as has been done extensively for nearby galaxies and also for different samples of galaxies at redshifts up to $z \sim 2$ in different ways (e.g. Reddy et al. 2010; Yoshikawa et al. 2010; Kashino et al. 2013; Wuyts et al. 2013; Price et al. 2014; Reddy et al. 2015; De Barros et al. 2016). We find a high attenuation of the Balmer lines, with $A_V = 2.90 \pm 0.58$, whereas the "energy balance" between the IR and the UV, that is, L_{IR}/L_{UV}, yields a lower attenuation $A_V = 1.58^{+0.30}_{-0.10}$ (cf. Tables 1 and 2). The ratio of the A_V values derived in this way is ~ 0.5, comparable to that of classical studies of low-redshift galaxies (cf. Calzetti et al. 2000). Adopting the Galactic extinction law (Cardelli et al. 1989), we obtain a some-

what lower $A_V = 2.26 \pm 0.45$, marginally higher that the value from the "energy balance". Such differences between the nebular and stellar attenuation have also been found at $z \sim 1 - 2$, for example by Yoshikawa et al. (2010) and Price et al. (2014). Reddy et al. (2015) and De Barros et al. (2016) argue that this difference increases with increasing SFR of the galaxies, thus reconciling earlier studies with apparently discrepant conclusions on the nebular and stellar color excess. The exact physical explanation for these observed differences between stellar and nebular attenuation and their dependence on galaxy properties (e.g., on SFR, sSFR, age and others) are still debated (see e.g. Price et al. 2014; Reddy et al. 2015, for conflicting views).

Finally we note that the attenuation of A68-HLS115 is fairly high, with an $A_V \sim 1.6 - 3$. The observed Balmer decrement indeed corresponds to an attenuation of Hα by a factor of approximately ten. Although high, this attenuation is quite consistent with expectations from the average relation between A_V and stellar mass, which is found by numerous studies for galaxies at least out to $z \sim 3$ (cf. Dominguez et al. 2013; Price et al. 2014; Álvarez-Márquez et al. 2016). It should also be recalled that our source has been selected from the IR, which should favor dusty galaxies.

5.2. Metallicity and metallicity gradient

We can use two metallicity indicators in our galaxy: N2 using [NII]/Hα and O3N2 using [NII]/Hα and [OIII]/Hβ. They both lead to a consistent oxygen abundance of 8.58 ± 0.07 and 8.52 ± 0.10 (see Table 2), respectively, when using the indicators from Pettini & Pagel (2004).

Figure 3 (top panel) shows the oxygen abundance gradient as a function of radius obtained using the N2 indicator. It has been derived at three different radii by fitting elliptical annuli on the velocity map in the source plane with the method of Krajnović et al. (2006). By averaging metallicity values of all the spaxels in the annuli, we obtain a slightly negative metallicity gradient (higher metallicity in the core than in outer regions) of -0.057 ± 0.070 dex in total (or -0.014 ± 0.016 dex kpc^{-1}) although with a low significance. This is consistent with observations at high redshift which show generally flat or negative gradients (e.g. Jones et al. 2013; Stott et al. 2014). However, it is now known that the spatial resolution and annular binning can have an impact on the obtained metallicity gradient (Yuan et al. 2013; Mast et al. 2014). Indeed, since our observations are seeing-limited and considering that the FWHM of the PSF varies between 1 and 5 kpc depending on the orientation, the observed

metallicity gradient could be flattened by these effects. Using only three annuli to determine the gradient could also cause a flatter gradient.

Moreover, our metallicity gradient is similar to gradients found in galaxies with the same stellar mass and sSFR as shown in Fig. 3 (middle and bottom panels). We include data from Swinbank et al. (2012), Stott et al. (2014), and Wuyts et al. (2016), and the relation obtained by Stott et al. (2014) (in orange) for comparison. No correlation is seen with the stellar mass. However, Wang et al. (2017) observe a tentative anti-correlation between stellar mass and metallicity gradient, coherent with a scenario where more massive galaxies are more evolved. Stott et al. (2014) find a trend with the sSFR while combining their data with those of Rupke et al. (2010), Queyrel et al. (2012), and Swinbank et al. (2012), which could imply that the sSFR is driven by the amount of gas flowing towards the center. Using simulations, Sillero et al. (2017) find in a recent study that a correlation between the metallicity gradient and sSFR is seen in certain conditions when strong gas inflows are produced by interactions or instabilities. However, when adding the data from Wuyts et al. (2016), this trend becomes less obvious, which could mean that the gas flowing to the center might not be the only physical process that influences the sSFR.

5.3. Kinematics

Figure 4 (left panel) presents the velocity map in the source plane centered on the redshift obtained from the Hα emission line of the integrated spectrum. The map shows an obvious velocity gradient. To model the kinematics, we use a markov-chain Monte Carlo (MCMC) method to fit the observed velocity map with the PSF convolved model. We adopt the arctangent function for the velocity profile (Courteau 1997), which has been used in many studies (e.g., Jones et al. 2010):

$$v(r) = v_{rot}\frac{2}{\pi}\arctan\frac{r}{r_t}, \qquad (3)$$

where r is the radius, r_t is the turnover radius, and v_{rot} is the maximum rotation velocity. All the parameters are free to vary when fitting the model. The fit is performed in the source plane. The model velocity map obtained is shown in Fig. 4 (middle panel) and the kinematic properties obtained are presented in Table 2.

The rotation curve determined from the reconstructed Hα velocity map in the source plane and from the kinematic model is presented in Fig. 5. The curve in red indicates the intrinsic rotation curve, corrected for the inclination. The rotation curve reveals a rotating disk typical of star-forming galaxies on the MS (e.g., Förster Schreiber et al. 2009; Wisnioski et al. 2015).

The observed velocity dispersion map is shown in Fig. 4 (right panel). The intrinsic velocity dispersion is measured in spaxels on the major axis in the outer region of the disk to avoid beam smearing as much as possible and is also corrected for the instrumental broadening following Eq. 2. From Burkert et al. (2016) and Johnson et al. (2018), we know that even if we take the measurement in the outer region, there is still an increase of the dispersion value due to the beam smearing, which is of 5-15% if we take into account the stellar mass and inclination of our galaxy. If we add this extra-correction for the beam smearing, we obtain an intrinsic velocity dispersion of $\sigma_0 \sim 80 \pm 10$ km s^{-1} (Table 2). This value is in agreement with an evolution of the intrinsic velocity dispersion with redshift, where galaxies at high redshift show a higher intrinsic velocity dispersion compared to the local galaxies (e.g. Wisnioski et al. 2015; Turner

et al. 2017; Girard et al. 2018). This value is nevertheless higher compared to samples at $z = 1$ and $z = 2$ of Wisnioski et al. (2015), which show a mean dispersion of 25 and 50 km s^{-1}, respectively. This suggests that the high turbulence observed in our galaxy could be due to the high gas fraction of $f_{gas} = 0.75 \pm 0.15$ of this source. Moreover, the observed velocity dispersion map does not show any evidence of a peak in the kinematic center. An increase of the velocity dispersion in the center can be an indication of a rotating disk according to Rodrigues et al. (2017). However, this increase is lower for galaxies with high velocity dispersion (> 70 km s^{-1}) and could explain why we do not see this effect here (Johnson et al. 2018).

We obtain a ratio $v_{rot}/\sigma_0 = 2.73$, meaning that the galaxy is dominated by rotation if we use the typical criterion of $v_{rot}/\sigma_0 > 1$ (e.g. Wisnioski et al. 2015; Mason et al. 2017; Turner et al. 2017; Girard et al. 2018), but this ratio also indicates that the disk is marginally stable. This value is typical at $z \sim 1.6$ according to the stability (v_{rot}/σ_0) evolution relation with redshift obtained by Wisnioski et al. (2015), and our galaxy is in good agreement with the trends they find where the stability (v_{rot}/σ_0) is correlated to sSFR and f_{gas}. Indeed, they get a lower stability ($v_{rot}/\sigma_0 \lesssim 3$) at high sSFR ($\gtrsim 2$ Gyr^{-1}) and f_{gas} ($\gtrsim 0.5$). This is fully in line with the v_{rot}/σ_0, sSFR, and f_{gas} measured in A68-HLS115. This suggests that the disk turbulence and instability in this galaxy are mostly regulated by incoming gas (available gas reservoir for star formation).

Moreover, the Toomre stability criterion (Toomre 1964) can be expressed as

$$Q_{crit} = \sqrt{2}\frac{\sigma_0}{v_{rot} f_{gas}}. \qquad (4)$$

We obtain for our galaxy a direct measurement of $Q_{crit} = 0.70$. A value of $Q_{crit} = 1$ is expected for a *thin* quasi-stable gas disk and $Q_{crit} < 1$ is an indication of an unstable system that can fragment into clumps (e.g. Jones et al. 2010). However, the critical value of the Toomre parameter for a *thick* gas disk is $Q_{crit} = 0.67$ (Kim & Ostriker 2007), which could be the case of A68-HLS115 since several studies point out that disk galaxies at $z \sim 1 - 2$ are thick (e.g. Genzel et al. 2011). White et al. (2017) also obtain a linear correlation between σ_0/v_{rot} and f_{gas} from Eq. 4. From this relation and assuming hydrostatic equilibrium and that the pressure is caused only by the turbulent motions of the gas, they find that a higher gas fraction leads to thicker disks in marginally stable disks.

5.4. Properties of the clumps

The Hα and [NII]/Hα maps of A68-HLS115 in the source plane are presented in Fig. 6. We are able to identify three clumps in the image plane of the Hα map with CLUMPFIND (Williams et al. 1994) using a selection criterion of $\geq 3\sigma$. Overlaid on the observed HST/F814W images with dashed white lines (see Fig. 1), we see that these Hα clumps are blends of multiple smaller star-forming clumps resolved in the HST image. The Hα clumps are exclusively distributed over the eastern part of the galaxy, while no Hα clump is detected in the western part yet holding one of the most prominent HST clumps. When looking in the source plane after the reconstruction, we find that the Hα clumps as well as the clumps observed in the HST images could trace a spiral structure. This scenario would be consistent with the observed velocity map which is typical of a rotating disk.

We combine all the spaxels within each clump and obtain individual spectra. We fit the Hα and [NII] emission lines in the
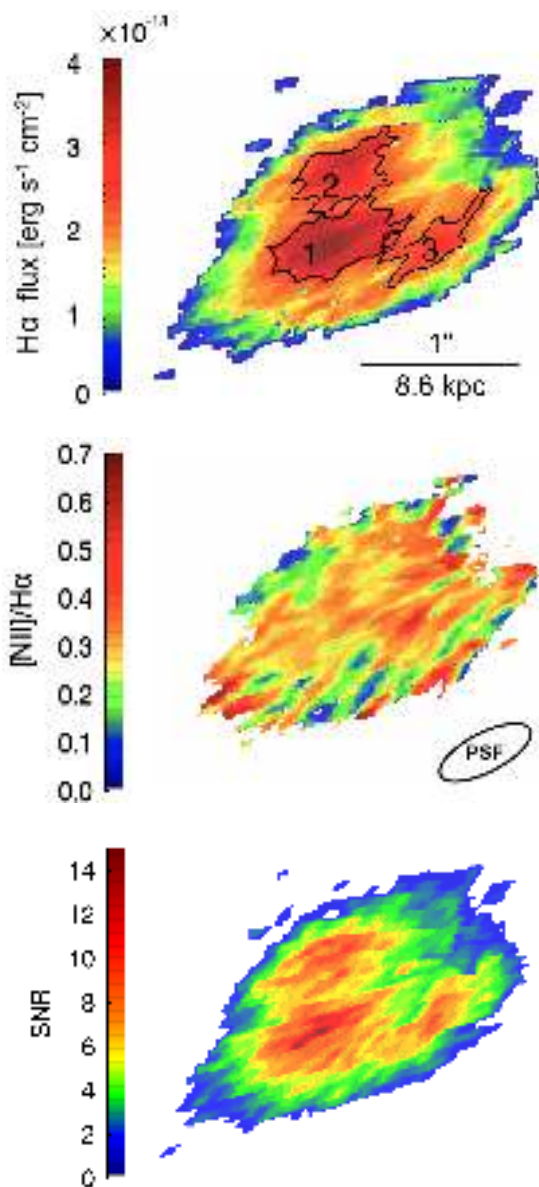
Table 3: Clump properties.

Parameters	Clump 1	Clump 2	Clump 3
$\text{SFR}_{H\alpha}{}^{a}$ [$M_\odot \text{yr}^{-1}$]	41 ± 3	24 ± 2	10 ± 1
Radius^{b} [kpc]	1.57	1.34	≤ 1.26
$12 + \log(\text{O/H})_{N2}$	8.60 ± 0.07	8.58 ± 0.07	8.60 ± 0.08
$12 + \log(\text{O/H})_{O3N2}$	8.55 ± 0.11	-	-
$12 + \log(\text{O/H})_{O3N2,H\alpha}{}^{c}$	8.58 ± 0.08	8.52 ± 0.08	8.60 ± 0.09
σ [km s^{-1}]	92 ± 2	97 ± 3	101 ± 3
$\sigma_{\text{med}}{}^{d}$ [km s^{-1}]	90 ± 2	95 ± 1	101 ± 2

Notes.
[a] The SFR has been corrected for lensing and for the dust attenuation using the extinction measured from the integrated spectrum.
[b] The radius corresponds to $\sqrt{a \times b}$, where a and b are the semi-major and semi-minor axis. The typical error on the size of the clump is about 10%.
[c] Since the Hβ emission line is only detected in the clump 1, the Hβ flux has been derived from the Hα flux using a Hα/Hβ ratio of 2.86 and the A_V measured from the integrated spectrum.
[d] σ_{med} is the median dispersion value of the spaxels inside each clump. The errors correspond to 95% confidence range.

of ~ 11 km s^{-1} between clump 1 and 3. Overall, the clumps show a similar metallicity, a similar velocity dispersion as in the rest of the disk (see Table 2), and seem to be embedded in the rotating disk.

Livermore et al. (2015) show an evolution of the clump surface brightness with higher values at high redshift compared to local HII regions. The three clumps follow this trend with an SFR$_{H\alpha}$ about 100 times higher than what we find in the local Universe for clumps with similar size according to the relation obtained by Livermore et al. (2015) at $z = 0$ using the SINGS survey (Kennicutt et al. 2003). We also find that the three clumps contribute individually to $5 - 20\%$ on the SFR$_{H\alpha}$ of the whole galaxy. Therefore, the majority ($\sim 63\%$) of the observed $H\alpha$ flux is found outside these regions. Similarly, Guo et al. (2012) obtain SFRs of $\sim 10\%$ and $\sim 50\%$ for individual clumps and total contribution, respectively, for star-forming galaxies at $z \sim 2$ with SFR measured through SED fitting.

For clump 1 we can measure the Balmer decrement (Hα/Hβ=8) , which turns out to be higher than that measured from the integrated spectrum. The attenuation of clump 1 is therefore quite high, $A_V = 3.6$, showing that at least this clump does not correspond to a region which is visible due to inhomogeneities in the dust distribution, which could mimic stellar and ionized gas clumps, as suggested by Buck et al. (2017). We therefore conclude that this "clump" (region) does most likely indeed correspond to some physical concentration of ionized gas (HII region(s)), which is primarily powered by one or several young stellar clusters, and that such physical entities truly form in high-redshift galaxies.

6. Conclusions

We have presented new observations of A68-HLS115 at $z = 1.5858$, a star-forming galaxy located behind the galaxy cluster Abell 68, but strongly lensed by a cluster galaxy member, with SINFONI, a NIR IFU at the VLT. We detect Hα, Hβ, [NII], and [OIII] emission lines. Combined with images covering the B band to the FIR and CO(2-1) observations, this makes this galaxy one of the only sources for which such multi-band observations are available and for which it is possible to study the
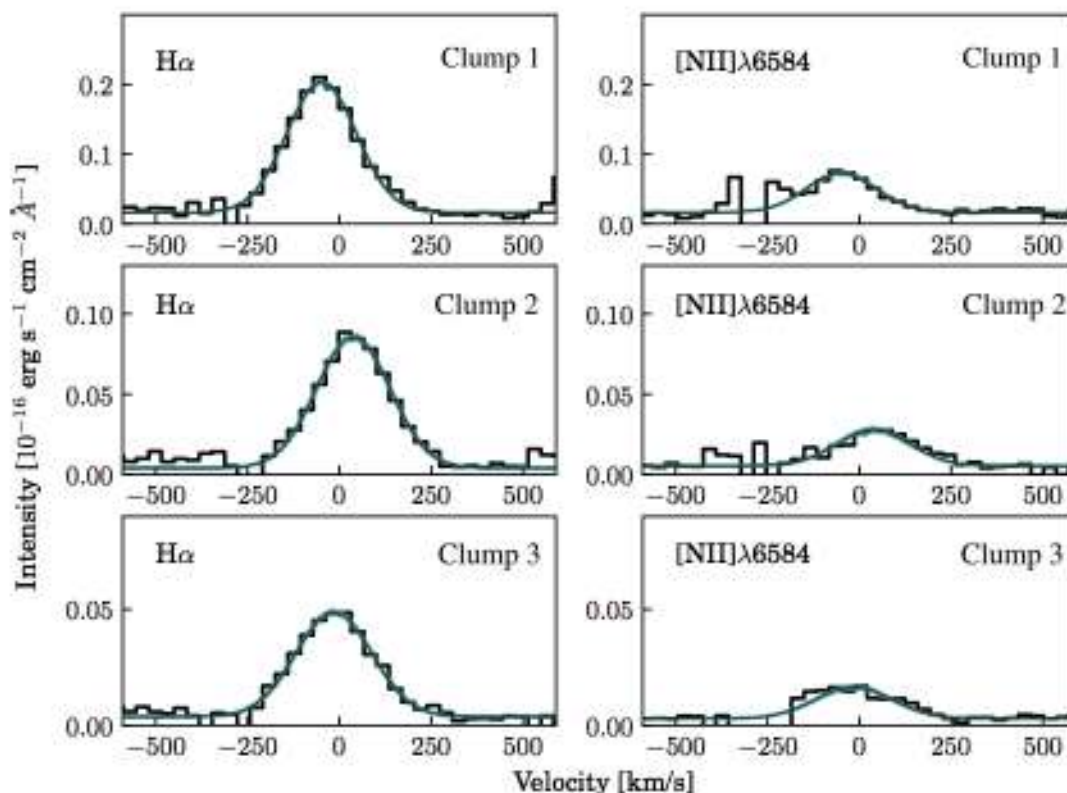
Fig. 6: Hα flux per spaxel (top panel), [NII]/Hα line ratio (middle panel), and S/N (bottom panel) in the source plane. The black contours represent the Hα clumps.

same way as the integrated spectrum (see Sect. 4.2) for each clump (see Fig. 7). For the brightest clump (clump 1), it is also possible to fit the [OIII] and Hβ emission lines. As a result, we obtain the total flux of each emission line for each clump, the SFR$_{H\alpha}$ assuming a uniform extinction correction derived from the integrated spectrum, the oxygen abundance using the N2 and O3N2 indicators from Pettini & Pagel (2004), for which we use the Hα flux to derive the Hβ flux, and the velocity dispersion corrected for the instrumental broadening. Since the velocity dispersions can be affected by beam smearing, we also measure the median dispersion value per clump using the velocity dispersion map. Indeed, this effect is less important for the measurement of individual spaxels. The main properties of the clumps are summarized in Table 3.

We get a very similar metallicity for each clump using the N2 indicator, while using the O3N2 we get a value slightly lower for clump 2, but the difference is not significant. We also get a high velocity dispersion for our three clumps, with a difference

Fig. 7: Hα and [NII] emission line intensities as a function of the velocity for the three clumps. The zero velocity corresponds to the redshift obtained with the Hα emission line from the integrated spectrum. The 1000 realizations obtained with the Monte Carlo simulation are shown in blue and the final result is shown in black.

properties of resolved clumps and to perform a detailed analysis of the integrated properties, kinematics, and metallicity. This source is also one of the most gas-rich galaxies ($f_{gas} = 75\%$) known at $z > 1$.

A68-HLS115 is a dusty and gas-rich galaxy with a stellar mass $M_\star \sim 3 \times 10^{10}$ M$_\odot$ and a star formation rate SFR $\sim 80 - 120$ M$_\odot$ yr^{-1}, as measured from the UV, IR, and from SED fits (Table 1). Comparing the attenuation from Balmer decrement with that derived from the UV and IR luminosity, we find a higher attenuation for the nebular lines compared to the stellar continuum, as found for several other galaxies at high redshift (e.g. Yoshikawa et al. 2010; Shivaei et al. 2016).

The galaxy shows a velocity map typical of rotating galaxies and we obtain a high intrinsic velocity dispersion of 80 ± 10 km s^{-1}. The stability ratio of $v_{rot}/\sigma_0 = 2.73$ is characteristic of galaxies at high redshift with a high sSFR and gas fraction and suggests that the disk is marginally stable. We obtain a direct measurement of the Toomre stability criterion of $Q_{crit} = 0.70$, which could suggest the presence of a thick gas disk. We also find a slightly negative metallicity gradient.

We are able to identify three clumps in the Hα map that show similar metallicity and velocity dispersion to one another, but also to the host galaxy, and that seem embedded in the rotating disk. We obtain star formation rate densities approximately 100 times higher than what is found for HII regions in the local Universe. Finally, the clumps in our galaxy represent $\sim 40\%$ of the SFR$_{H\alpha}$ of the whole galaxy.

For one of the Hα clumps, we can measure the extinction from the Balmer decrement, finding an extinction which is higher than the average over the entire galaxy. This shows that at least this clump is not just an appearance caused by inhomogeneities in the dust distribution of the interstellar medium, as suggested by Buck et al. (2017) for the stellar or ionized gas clumps frequently observed at high redshift.

References

Adamo, A., Östlin, G., Bastian, N., et al. 2013, ApJ, 766, 105
Álvarez-Márquez, J., Burgarella, D., Heinis, S., et al. 2016, A&A, 587, A122
Bournaud, F., Perret, V., Renaud, F., et al. 2014, ApJ, 780, 57
Buck, T., Macciò, A. V., Obreja, A., et al. 2017, MNRAS, 468, 3628
Burkert, A., Förster Schreiber, N. M., Genzel, R., et al. 2016, ApJ, 826, 214
Cañameras, R., Nesvadba, N., Kneissl, R., et al. 2017, A&A, 604, A117
Calzetti, D., Armus, L., Bohlin, R. C., et al. 2000, ApJ, 533, 682
Cardelli, J. A., Clayton, G. C., & Mathis, J. S. 1989, ApJ, 345, 245
Cava, A., Schaerer, D., Richard, J., et al. 2018, Nature Astronomy, 2, 76
Chabrier, G. 2003, PASP, 115, 763
Courteau, S. 1997, AJ, 114, 2402
Cowie, L. L., Hu, E., & Songaila, A. 1995, AJ, 110, 1576
Daddi, E., Dickinson, M., Morrison, G., et al. 2007, ApJ, 670, 156
De Barros, S., Reddy, N., & Shivaei, I. 2016, ApJ, 820, 96
Dekel, A., Sari, R., & Ceverino, D. 2009, ApJ, 703, 785

Dessauges-Zavadsky, M., Schaerer, D., Cava, A., Mayer, L., & Tamburello, V. 2017, ApJ, 836, L22

Dessauges-Zavadsky, M., Zamojski, M., Schaerer, D., et al. 2015, A&A, 577, A50

Dominguez, A., Siana, B., Henry, A. L., et al. 2013, ApJ, 763, 145

Elmegreen, B. G., Elmegreen, D. M., Fernandez, M. X., & Lemonias, J. J. 2009, ApJ, 692, 12

Elmegreen, D. M., Elmegreen, B. G., Ravindranath, S., & Coe, D. A. 2007, ApJ, 658, 763

Förster Schreiber, N. M., Genzel, R., Bouché, N., et al. 2009, ApJ, 706, 1364

Förster Schreiber, N. M., Shapley, A. E., Genzel, R., et al. 2011, ApJ, 739, 45

Genzel, R., Newman, S., Jones, T., et al. 2011, ApJ, 733, 101

Girard, M., Dessauges-Zavadsky, M., Schaerer, D., et al. 2018, A&A, 613, A72

Gray, R. O. & Corbally, C. J. 1994, AJ, 107, 742

Guo, Y., Giavalisco, M., Ferguson, H. C., Cassata, P., & Koekemoer, A. M. 2012, ApJ, 757, 120

Johnson, H. L., Harrison, C. M., Swinbank, A. M., et al. 2018, MNRAS, 474, 5076

Jones, T., Ellis, R. S., Richard, J., & Jullo, E. 2013, ApJ, 765, 48

Jones, T. A., Swinbank, A. M., Ellis, R. S., Richard, J., & Stark, D. P. 2010, MNRAS, 404, 1247

Kashino, D., Silverman, J. D., Rodighiero, G., et al. 2013, ApJ, 777, L8

Kennicutt, Jr., R. C. 1998, ARA&A, 36, 189

Kennicutt, Jr., R. C., Armus, L., Bendo, G., et al. 2003, PASP, 115, 928

Kim, W.-T. & Ostriker, E. C. 2007, ApJ, 660, 1232

Krajnović, D., Cappellari, M., de Zeeuw, P. T., & Copin, Y. 2006, MNRAS, 366, 787

Kurucz, R. L. 1993, VizieR Online Data Catalog, 6039

Leethochawalit, N., Jones, T. A., Ellis, R. S., et al. 2016, ApJ, 820, 84

Livermore, R. C., Jones, T., Richard, J., et al. 2012, MNRAS, 427, 688

Livermore, R. C., Jones, T. A., Richard, J., et al. 2015, MNRAS, 450, 1812

Mandelker, N., Dekel, A., Ceverino, D., et al. 2017, MNRAS, 464, 635

Mason, C. A., Treu, T., Fontana, A., et al. 2017, ApJ, 838, 14

Mast, D., Rosales-Ortega, F. F., Sánchez, S. F., et al. 2014, A&A, 561, A129

Patrício, V., Richard, J., Carton, D., et al. 2018, MNRAS, 477, 18

Pettini, M. & Pagel, B. E. J. 2004, MNRAS, 348, L59

Price, S. H., Kriek, M., Brammer, G. B., et al. 2014, ApJ, 788, 86

Puglisi, A., Daddi, E., Renzini, A., et al. 2017, ApJ, 838, L18

Queyrel, J., Contini, T., Kissler-Patig, M., et al. 2012, A&A, 539, A93

Reddy, N. A., Erb, D. K., Pettini, M., Steidel, C. C., & Shapley, A. E. 2010, ApJ, 712, 1070

Reddy, N. A., Kriek, M., Shapley, A. E., et al. 2015, ApJ, 806, 259

Richard, J., Kneib, J.-P., Jullo, E., et al. 2007, ApJ, 662, 781

Richard, J., Smith, G. P., Kneib, J.-P., et al. 2010, MNRAS, 404, 325

Rodighiero, G., Cimatti, A., Gruppioni, C., et al. 2010, A&A, 518, L25

Rodrigues, M., Hammer, F., Flores, H., Puech, M., & Athanassoula, E. 2017, MNRAS, 465, 1157

Rupke, D. S. N., Kewley, L. J., & Chien, L.-H. 2010, ApJ, 723, 1255

Salmi, F., Daddi, E., Elbaz, D., et al. 2012, ApJ, 754, L14

Salpeter, E. E. 1955, ApJ, 121, 161

Schaerer, D., de Barros, S., & Sklias, P. 2013, A&A, 549, A4

Shivaei, I., Kriek, M., Reddy, N. A., et al. 2016, ApJ, 820, L23

Sillero, E., Tissera, P. B., Lambas, D. G., & Michel-Dansac, L. 2017, MNRAS, 472, 4404

Sklias, P., Zamojski, M., Schaerer, D., et al. 2014, A&A, 561, A149

Stott, J. P., Sobral, D., Swinbank, A. M., et al. 2014, MNRAS, 443, 2695

Swinbank, A. M., Papadopoulos, P. P., Cox, P., et al. 2011, ApJ, 742, 11

Swinbank, A. M., Smail, I., Sobral, D., et al. 2012, ApJ, 760, 130

Tamburello, V., Mayer, L., Shen, S., & Wadsley, J. 2015, MNRAS, 453, 2490

Tamburello, V., Rahmati, A., Mayer, L., et al. 2017, MNRAS, 468, 4792

Toomre, A. 1964, ApJ, 139, 1217

Turner, O. J., Cirasuolo, M., Harrison, C. M., et al. 2017, MNRAS, 471, 1280

Wang, X., Jones, T. A., Treu, T., et al. 2017, ApJ, 837, 89

White, H. A., Fisher, D. B., Murray, N., et al. 2017, ApJ, 846, 35

Williams, J. P., de Geus, E. J., & Blitz, L. 1994, ApJ, 428, 693

Wisnioski, E., Förster Schreiber, N. M., Wuyts, S., et al. 2015, ApJ, 799, 209

Wisnioski, E., Glazebrook, K., Blake, C., et al. 2012, MNRAS, 422, 3339

Wuyts, E., Rigby, J. R., Gladders, M. D., et al. 2012, ApJ, 745, 86

Wuyts, E., Wisnioski, E., Fossati, M., et al. 2016, ApJ, 827, 74

Wuyts, S., Förster Schreiber, N. M., Nelson, E. J., et al. 2013, ApJ, 779, 135

Yoshikawa, T., Akiyama, M., Kajisawa, M., et al. 2010, ApJ, 718, 112

Yuan, T.-T., Kewley, L. J., & Rich, J. 2013, ApJ, 767, 106

A Tale of Two Clump Masses: A new way to study clump formation in simulations

S. M. Benincasa,[1]★ J. W. Wadsley,[1] H. M. P. Couchman,[1] A. R. Pettitt[2] and E. J. Tasker

[1]*Department of Physics & Astronomy, McMaster University, 1280 Main St. W, Hamilton L8S 4K1, Canada*

[2]*Department of Physics, Faculty of Science, Hokkaido University, Sapporo 060-0810, Japan*

[3]*Institute of Space and Astronautical Science, Japan Aerospace Exploration Agency, Yoshinodai 3-1-1, Sagamihara, Kanagawa 252-5210, Japan*

ABSTRACT

We present a new method to study the characteristic scales of collapse and fragmentation in galactic disks. Clump formation is seeded in simulations via controlled perturbations with a specified wavelength and velocity. These are applied to otherwise quiet gas disks ranging from analogues of present day spirals to gas-rich, high-redshift galaxies. The results are compared to linear theory, turbulently perturbed disks and observations. The results reflect the expectations of linear, non-axisymmetric theory with a finite window for growth into a bound clump. We identify two new modes of clump formation: rotation-driven fission and fragmentation of tidal tails, though both are expected to rarely contribute to clump formation in observed disks. We find that bound clumps are generally much smaller than the so-called Toomre mass. The preferred scale for fragmentation increases with the disk gas mass but cannot produce bound objects larger than $\sim 10^9$ M$_\odot$. The most likely bound clump mass increases from 3×10^6 in low mass disks up to 5×10^8 M$_\odot$. We conclude that observed massive stellar and gaseous clumps on 1 kpc scales at high redshift are most likely aggregates of many initially distinct bound clumps.

Key words: methods: numerical – stars: formation – ISM: clouds – galaxies: ISM – galaxies: star formation – galaxies: high-redshift

1 INTRODUCTION

The typical size of star clusters must, to some degree, be dependant on the galactic environment. This dependance can manifest itself in different ways. The Jeans' mass, which changes based on environment, plays a role (e.g. Hopkins 2012). The pressure likely plays a role; high pressure environments such as Arp 220 have larger star clusters when compared to other local galaxies (e.g. Wilson et al. 2006). If we begin by considering low redshift galaxies, a preferred mass-scale for star cluster formation is apparent. In the Milky Way itself, star clusters have typical masses between $10^3 - 10^4$ M$_\odot$ (Fall & Chandar 2012). A preferred scale for star clusters may in turn suggest a preferred scale for Giant Molecular Clouds (GMCs). In the Milky Way GMCs have typical masses between $10^5 - 10^6$ M$_\odot$ and typical sizes of 50 - 100 pc (Fukui & Kawamura 2010; McKee & Ostriker 2007).

If we consider galaxies at higher redshifts, these preferred scales appear to change. Stellar observations are able to identify large UV-bright star-forming regions called *clumps* (Elmegreen et al. 2007). The CANDELS survey has

provided extensive clump catalogues for galaxies between $0.5 < z < 3.5$. The properties of clumps identified in CANDELS galaxies suggest they are extremely large, with typical masses of $10^7 - 10^9$ M$_\odot$ and typical sizes ~ 1 kpc (Guo et al. 2015, 2018). Other compilation studies find masses between $10^5 - 10^9$ M$_\odot$ (Dessauges-Zavadsky & Adamo 2018). Either way, these are orders of magnitude more massive than present-day clusters or star-forming regions.

This picture is even more complex if we add in starbursts or merger-driven systems. As mentioned above, if we consider Arp 220, there are many active sites of star formation and the star-forming complexes may be much larger than those in the Milky Way (Murray et al. 2010, and references therein). In these environments the masses of stellar clusters increase dramatically. Wilson et al. (2006) find masses approaching 10^7 M$_\odot$, which may make them candidates for young globular clusters.

The conditions in star-forming regions should be imprinted in the properties of gas. At higher redshifts, and in starburst systems, the conditions both within and around galaxies were different than at low redshift. Specifically, at higher redshifts the galaxy interaction rate was higher and galaxies themselves are much more likely to be gas rich.

★ E-mail: benincsm@mcmaster.ca

It is no surprise that in such gas-rich, highly molecular environments the properties of star-forming regions are likely to be different. Indeed, the appearance of gas disks beyond z∼0.5 are much more clumpy in nature (e.g. Förster Schreiber et al. 2009). This highly molecular clumpy nature may suggest that star-forming regions may be larger in both mass and spatial extent. Wide beam observational studies suggest these objects have masses between 10^8 - 10^{10} M$_\odot$, or approximately $1 - 10\%$ of the total disk mass (e.g. Tacconi et al. 2010; Swinbank et al. 2010, 2011; Genzel et al. 2011; Hodge et al. 2012). The corresponding physical sizes range from as small as 100 pc to as large as 2 kpc (e.g. Swinbank et al. 2010; Tacconi et al. 2010).

However, recent results from the SGASS lensing survey have shown a finer level of substructure, albeit in galaxies less massive than those typical in the CANDELS sample (Johnson et al. 2017a). These results show that stellar clump sizes can be consistent with present-day star clusters, which would originate from objects similar to present day GMCs with high star formation efficiency (Johnson et al. 2017b; Rigby et al. 2017). Another such lensing study has been done in the Cosmic Snake (Cava et al. 2018). Using data from the CLASH survey, the authors have obtained both a lensed arc and counterimage. In this way they can compare two spatial resolutions for the same object. They find that the lower resolution image (counterimage) produces clumps that are amplified by a factor of 2-5 on average, for an decrease in resolution of 10 times. Studies like these suggest two important points. First, the gas mass of a galaxy is important for determining the scale of star formation. Second, the resolution of earlier studies may not be sufficient to resolve clumps.

With the typical physical resolution of instruments at high redshift being generally poorer, it may be that we are treating collections of GMCs (Tacconi et al. 2010) as a single entity. This idea has been lent credence by samples of lensed galaxies: while directly observed galaxies are often large due to selection effects, lensed galaxies are typically of lower mass (M$_\star \sim 10^9$ M$_\odot$). They provide us with a better resolved picture of the molecular gas. For example, Swinbank et al. (2010) find gas clumps of similar size to Milky Way GMCs, approximately 100 pc. They propose that these objects would be similar to present-day star-forming regions except with more star-forming cores with higher densities. Hodge et al. (2012) infer typical internal densities of ~ 100 cm^{-3}, in accordance with the typical density of low-redshift GMCs. If we infer masses from these sizes, we can assume that these objects would likely have masses similar to large present-day GMCs: maybe between $10^5 - 10^7$ M$_\odot$. Local starburst galaxies with enhanced star-formation and kinematic properties similar to galaxies at z ∼ 1.5 can also be used as a testbed for these theories. Their proximity offers better resolution studies and HST-DYNAMO has studied 13 such galaxies (White et al. 2017). Studies here confirm that clump clustering is likely to impact the measurement of clump properties at higher redshifts, where resolution degrades (Fisher et al. 2017).

If we look to isolated galaxy simulations, we see results consistent with small star-forming regions. For example, (Tamburello et al. 2015) find smaller clump masses (< 10^7 M$_\odot$). The higher resolution available in isolated galaxy simulations also offers the perfect place to study the impacts of

resolution on structure identification. Some work has suggested that the resolution of HST at the redshifts concerned is insufficient to fully resolve these clumpy objects. Tamburello et al. (2017) and Dessauges-Zavadsky et al. (2017) have argued that at the spatial resolution of 1 kpc, it is not possible to fully resolve these stellar clumps. This supports the idea that we are just seeing collections of smaller stellar clumps, clustered closely together. Indeed, Behrendt et al. (2016) have shown that closely clustered clumps could be confused for more massive objects with the resolution of surveys like CANDELS.

At the other extreme, it has been suggested that in massive, gas-rich galaxies the physics of clump formation changes with Violent Disk instabilities (VDI) producing different outcomes (Dekel et al. 2009). This idea has been invoked to explain certain cosmological zoom simulations exhibiting larger clumps in the range 10^{7-9} M$_\odot$ (Mandelker et al. 2014, 2017). However, it has been theorized that not all gas rich disks host VDI, and that this behaviour is largely dependant on feedback strength rather than a qualitative difference in how clumps form (Fiacconi et al. 2017). Regardless, other studies of cosmological zoom simulations also report clump masses in this higher range (Agertz et al. 2009; Oklopčić et al. 2017) These larger clumps masses are seen not just in cosmological simulations, but in isolated galaxy simulations as well (Hopkins et al. 2012; Bournaud et al. 2014).

When comparing all of this data, we are faced with a seemingly inescapable difficulty. All of the studies discussed in the previously involve different methods. Some involve simulations on cosmological scales while others model isolated galaxies, the resolution of these two types of simulations can be quite different. Different studies use different numerical methods or different hydrodynamical schemes. Beyond that, perhaps the largest variable, is the type of feedback chosen. The type and strength of feedback chosen plays a large role in determining the structure of star-forming gas and, consequently, the structure of stellar clusters. All of these variables makes it incredibly confusing to compare results among different studies. Add on top of that the different types of observations we are considering, stellar versus gas, lensed versus un-lensed, and we are left with great difficulty in interpreting the results in the literature.

We propose a new method to study clump formation in simulations. Our method avoids the problems associated with many of the algorithm-specific assumptions discussed above. We seed clump formation events by hand and study their growth in high resolution isothermal disks that do not include feedback. In this way, we can constrain the initial mass of clumps formed in a variety of disks. These are directly comparable to both observationally determined masses and masses from theories of fragmentation.

The rest of the paper is laid out as follows. We begin by examining the predictions from linear theory in section 2. Linear theory is difficult to extrapolate to non-linear clumps properties. Instead, we use it to design simulations to explore clump formation in disks ranging from Milky Way-like cases to the heavy, turbulent disks expected at high redshifts. In section 3, we describe our controlled simulation approach which allows for high resolution and relatively easy interpretation of the results. We make first use of this in section 4, looking at isolated, turbulent disks. In order to study the

key scales for fragmentation and clump formation in a controlled way, we take a new approach of seeding non-linear perturbations. We present details of the approach and results in section 5. In section 6, we extrapolate from our simulation results to estimate likely clump masses based on disk conditions. Finally, in section 7 we discuss the observational implications of this study.

2 THEORETICAL EXPECTATIONS

While galactic disks are complex systems they are still amenable to theoretical analysis. The classic analysis by Toomre (1964) assumed a razor-thin, axi-symmetric system. This analysis applies in the case where the perturbations are effectively rings or very tightly wound (highly localized). In this case the dispersion relation has three main terms,

$$\omega^2 = \kappa^2 - 2\pi G\Sigma|k| + c_s{}^2 k^2. \tag{1}$$

The terms representing rotation (the epicycle frequency, κ) and pressure (the sound speed, c_s) act to stabilize the perturbations against gravity (Newtonian constant G) due to the underlying surface density Σ. As the physical scale, given by the wavenumber k, changes from large ($k \sim 0$) to small, we transition from being stabilized by rotation to sound waves or pressure; a stabilized regime is one in which the oscillation frequency, $\omega^2 > 0$. A key physical scale is the Toomre length,

$$\lambda_{\text{Toomre}} = \frac{4\pi^2 G\Sigma}{\kappa^2}. \tag{2}$$

Beyond this scale all perturbations are stabilized by shear (rotation). This sets a hard upper limit on the mass of clumps collapsing directly from a single perturbation. This can be translated into a mass, the Toomre mass, by assuming intrinsically circular collapsing regions,

$$M_{\text{Toomre}} = \pi \left(\frac{\lambda_{\text{Toomre}}}{2}\right)^2 \Sigma. \tag{3}$$

This mass is sometimes used an initial mass for clumps (Reina-Campos & Kruijssen 2017; Kruijssen 2012). However, this is somewhat ad hoc given that the linear dispersion relation applies to plane waves which would collapse to filaments or rings in the case of axi-symmetric global perturbations. So based on linear, axi-symmetric theory it is, at best, a rough guide.

At intermediate scales, $\lambda \sim \lambda_{\text{Toomre}}/2$, gravity is at its most effective and ω can be imaginary (unstable) if the Toomre Q parameter is less than one.

$$Q = \frac{c_s \kappa}{\pi G\Sigma} < 1. \tag{4}$$

The aforementioned violent disk instabilities are effectively non-linear Toomre instabilties. Thus the Toomre Q parameter should be a guide to locations where gas and stellar clumps can form (Inoue et al. 2016). It has been suggested that galaxies should be unstable in this mode until z~1-0.5 (Cacciato et al. 2012).

There are several complicating factors with applying these results directly to galactic disks. The first is that real disks are not razor thin. The primary impact is that disks can have Q as low as $\sim 2/3$ without being unstable to axisymmetric modes depending on how thick the disk is (Romeo

& Wiegert 2011). Secondly, galaxies are comprised of both gas and stars which act together and affect each other's individual stability (Goldreich & Lynden-Bell 1965a; Romeo et al. 2010; Agertz et al. 2015). Another limiting complication is that the linear theory is a local approximation and does not apply for structures that are comparable in size to the disk.

A key feature of these linear modes is that the growth rate is independent of both the amplitude and time so that for $\omega^2 < 0$ they are predicted to grow indefinitely so that finite disturbances may result. In other words, perturbations can grow indefinitely without being sheared apart.

A less commonly considered factor is the assumption of axi-symmetry or tight winding. It is widely recognized that disks grow large-scale perturbations (e.g. spiral structure) for supposedly stable Q-values in the range of 1-2. Secondly, the structures that grow are not axisymmetric. Axisymmetry greatly simplifies the dynamics as such perturbations do not elongate due to shear. Local non-axi-symmetric perturbations including the role of shear were examined by Goldreich & Lynden-Bell (1965b). In this case, the behaviour of plane waves does not simplify to a quadratic dispersion relation and even linear waves must be integrated as differential equations. Here we present the evolution equation for small amplitude surface density perturbations in the form given by Jog (1992), and simplified for the case of a single gaseous component,

$$\left(\frac{d^2\theta}{d\tau^2}\right) - \left(\frac{d\theta}{d\tau}\right)\left(\frac{2\tau}{1+\tau^2}\right) =$$
$$\frac{-\theta}{4A^2}\left[\kappa^2 + \frac{8AB}{1+\tau^2} - 2\pi G\Sigma k_y\sqrt{1+\tau^2} + c_s^2 k_y^2(1+\tau^2)\right], \tag{5}$$

where $\theta = \delta\Sigma/\Sigma$ is the fractional perturbation to the gas surface density, $\tau = 2At - k_x/k_y$ is a dimensionless time (such that the perturbation is radial at $\tau = 0$), Σ is the unperturbed surface density, κ is the epicycle frequency, A and B are the Oort constants, (k_x, k_y) is the wavevector, and c_s is the gas sound speed.

The terms in the square brackets are directly analogous to the terms in the axi-symmetric dispersion relation, Eqn. 2, and reduce to it in the appropriate limit. The first two terms represent shear and rotation but with an added time dependence associated with the instantaneous orientation of the wavefront. The latter terms depend on the instantaneous wavenumber which is sheared and thus minimized near $\tau = 0$. The pressure term always dominates for very early and late times.

Thus the behaviour of these linearized equations (in θ) is such that growth occurs briefly near $\tau \sim 0$ as the waves transition from leading to trailing, as noted by Goldreich & Lynden-Bell (1965b) and Jog (1992). The behaviour is oscillatory for other times. This means that the net growth is limited. Thus to achieve interesting outcomes from a relatively quiet start we must have multiple cycles of growth enabled by non-linear (e.g. wave to wave) interactions that reform leading waves. Put another way, to achieve bound structures we must start with substantial perturbations and grow these.

In the vigorously star forming disks of interest, we have feedback and turbulence to provide non-linear perturbations. For example, individual superbubbles sweep up mate-

rial on kpc scales. Interactions of many feedback events are expected to result in a turbulent velocity spectrum over a range of scales up to of order the disk scale height. Structure in the disk, such as pre-existing spiral modes, can also extract energy from the disk rotation to power turbulence on scales similar to the spiral waves themselves; this is comparable to the disk size for very unstable disks. Thus we would argue from the theory that the growth of finite, non-linear perturbations is a consistent picture of the development of bound clumps.

3   SIMULATION METHODS AND DISK MODELS

Astrophysical simulations always struggle to resolve the turbulent cascade and small scale structures developed through the coupling of turbulence and thermal instabilities. Taken from a broad perspective, however, turbulence behaves similarly to a polytropic gas. For this work, we have used isolated disks with an isothermal equation of state which is very simple to model relative to the full complexities of small scale turbulence. However, it directly provides the effective support we require of the turbulence and simultaneously provides a simple, straightforward model for the cooling losses. The effective equation of state of the ISM is complex but broadly similar to an isothermal one. In particular, Goldreich & Lynden-Bell (1965b) show that for equations of state with polytopic index $\gamma \sim 1$, non-linear unstable clumps will remain unstable and continue to collapse. Thus with this choice we can have confidence regarding the future fate of collapsing regions.

All of the disk simulations presented here use a static, logarithmic halo potential (Binney & Tremaine 2008) to represent the background of the dark matter halo, bulge and old stellar disk. This provides a well defined rotation curve (i.e. $\kappa(r)$). There is a small adjustment to this rotation curve due to the gas component. The gas surface density is exponential with a scale length of 5 kpc from 2 to 12 kpc with a smooth tailing off to zero below 2 kpc and beyond 12 kpc. Combined with a constant sound speed, this generates a Toomre Q that varies slowly in the active region from 2 to 12 kpc with a minimum value at ~ 5 kpc, and with values exceeding twice the minimum below 2 kpc and beyond 12 kpc.

We use the modern smoothed particle hydrodynamics code GASOLINE (Wadsley et al. 2004, 2017) to simulate the gas component, including self-gravity with a softening length of 10 pc. We have experimented with applying a Jeans floor that increases the effective pressure where the Jeans length is unresolved (following Robertson & Kravtsov 2008). However, we find that for the simulations discussed here this makes no difference to the amount of fragmentation. We do not directly apply a star formation or feedback model as these contain subgrid prescriptions that are code dependent. Additionally, there is still debate regarding the importance of different types of feedback (Murray et al. 2010; Hopkins et al. 2012).

We have built three disk models for this work and their properties are summarized in Table 1. These models cover a range of galaxy masses quoted in the literature: from a Milky Way sized galaxy to a galaxy that is massive enough to evolve into a present-day elliptical.

The first is modelled after a Milky Way-type disk, analogous to a less massive high redshift object (which we have labelled cold). It has a total gas mass of 6.95×10^9 M$_\odot$ and we use 5.56 million particles. The gas sound speed is 5 km/s, with a gas particle mass of 1250 M$_\odot$. These smaller mass objects are more typical of lensed samples, as here we are just sampling the galaxy luminosity function.

For the second disk (warm) we have modelled a more massive disk, which is a closer comparison to a high redshift turbulent, gas-rich disk. This case has a total gas mass of 1.96×10^{10} M$_\odot$. Here the gas sound speed is increased to 14 km/s to mimic the larger amount of turbulence present in high redshift galaxies (Förster Schreiber et al. 2009). To leave the effective resolution and Q parameter the same we then increase the gas particle mass to 3535 M$_\odot$.

Finally, the third disk (hot) is the most massive and warmest of the three. This case has a total gas mass of 5.56×10^{10} M$_\odot$. The gas sound speed is raised to 40 km/s. Again, to leave the effective resolution the same this results in a gas particle mass of 10^4 M$_\odot$. Galaxies in this higher mass range are more comparable to samples like that of Guo et al. (2018) for example. These galaxies which are already this massive at high redshift will likely become massive ellipticals by the present day.

Since we are interested in triggering clump formation, the surface density profiles chosen are such that the initial Toomre Q parameter lies near the border line of stability. We choose 5 kpc as the galactic radius of interest, where Q is at a minimum. At 5 kpc, the cold disk has an initial Q_{min} of 1.07, the warm disk has an initial Q_{min} of 1.15, and the hot disk has an initial Q_{min} of 1.1. The target value of Q was 1.1 but the effects of self gravity of the gas disk made it hard to get a precise Q, particularly for heavier disks.

For reference, a razor-thin disk stable to axisymmetric, linear perturbations has Q above 1. In other tests, not reported here, we find that for values above $Q \sim 1.3$, it is difficult for even fairly large perturbations to push regions toward gravitational instability. Since high-z galaxies have substantial inflows, we expect that they will always evolve to a point with Q between 1 and 1.3 so that clumps can form.

The Truelove criterion states that in a finite-difference code four cells are needed to resolve the Jean's length accurately (Truelove et al. 1997). A similar criterion exists in SPH simulations, where we require that the Jean's mass be greater than the neighbour number multiplied by the particle mass (Bate & Burkert 1997). We are able to resolve the Jean's mass up to 100 cm^{-3} in all of our disks, and up to 10^5 cm^{-3} two of our three disks. The disk in question is the coldest disk. We have resimulated higher resolution cases for a subset of our disks. In these cases we increase the resolution by splitting each gas particle eight times. In these high resolution cases we find no changes to the fragmentation or clump mass.

4   TURBULENT DISK SIMULATIONS

We begin by studying how turbulence can drive clump formation using full turbulent disk simulations. To create these cases, the entire disk is overlaid with a turbulent spectrum in a manner similar to Price & Federrath (2010). We ap-

Table 1. The three main disk initial conditions discussed in this work.

name	c_s	T	mass	$\Sigma_g(\text{R} = 5\text{ kpc})$	$Q_{\min}$	λ_{crit}	M_{Toomre}
cold disk	5.16 km/s	2 500 K	6.95 ×10^9 M$_\odot$	22 M$_\odot$/pc^2	1.07	960 pc	1.5 ×10^7 M$_\odot$
warm disk	14.59 km/s	20 000 K	1.96 ×10^{10} M$_\odot$	61.6 M$_\odot$/pc^2	1.15	2.4 kpc	2.9 ×10^8 M$_\odot$
hot disk	35.75 km/s	120 000 K	5.56 ×10^{10} M$_\odot$	176 M$_\odot$/pc^2	1.1	5.4 kpc	4.1 ×10^9 M$_\odot$
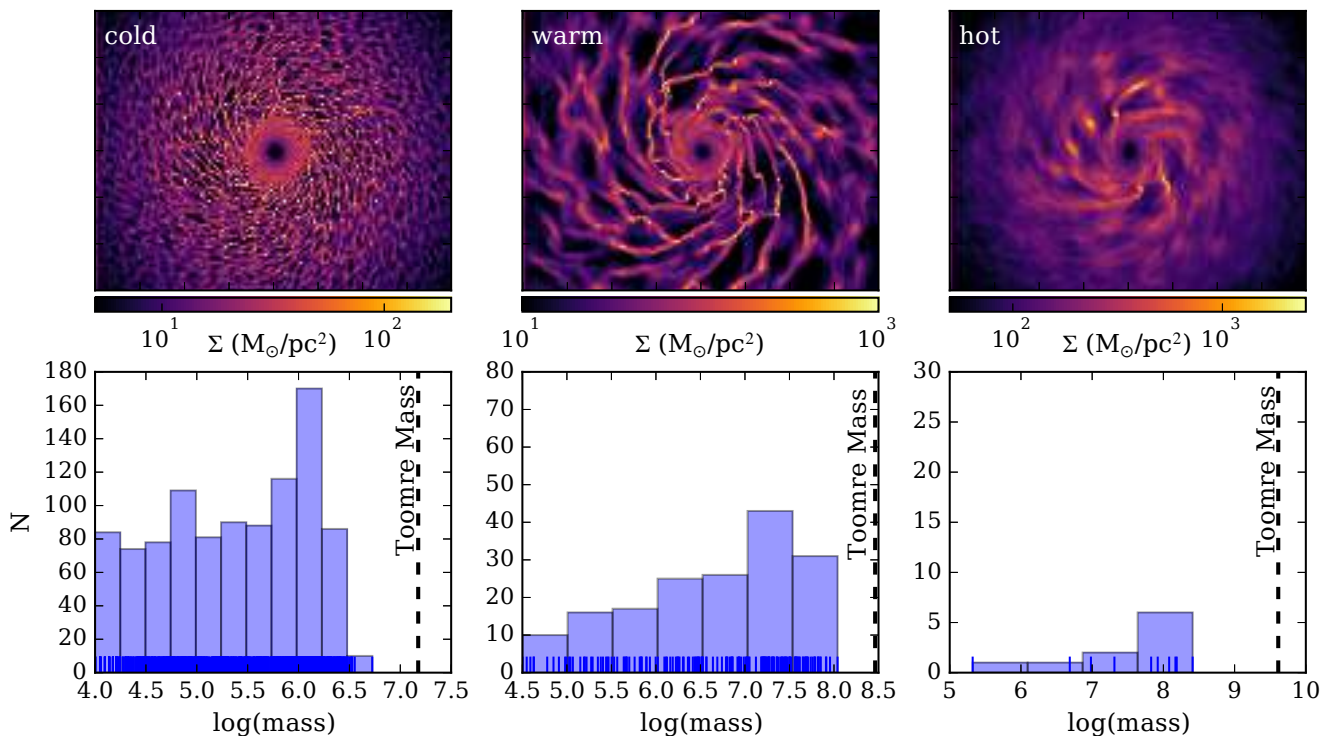
Figure 1. Mass distributions for clumps formed in the turbulent disks. *Top*: surface density maps of the disks at 40 Myr (this is the time at which all mass measurements are made). *Bottom*: clump mass distributions measured using SKID. The dashed line shows the Toomre mass for each case. In the distributions, the blue short lines show the masses of each of the clumps to illustrate how the clumps are distributed between the bins. As the mass of the disk is increased, the mass of the clumps formed likewise increases. In all cases the clumps formed are less massive than the Toomre mass, sometimes by an order of magnitude.

plied a Burgers' turbulent spectrum (k^{-4}) with a peak scale of 2 kpc to the initially quiet disks from Section 3. This gives an rms turbulent velocity of 7, 20 and 50 km/s in the cold, warm and hot disks, respectively. There is no stellar feedback to sustain the turbulence so it decays over a few crossing times. Results at time 40 Myr are shown in the left column of Figure 1, this is slightly more than twice the shear time (κ^{-1}). These disks are clearly visually clumpy, but we require a more quantitative measurement.

4.1 Measuring Clump Masses

For cases that are able to produce a clump structure, we must be able to assign a mass to these objects. We use two different approaches to assign clump masses. To study clump masses in manner similar to radio frequency observations (e.g. Colombo et al. 2014), we use the package astrodendro (Rosolowsky et al. 2008) to identify massive, dense structures in our simulations. As a second approach we use

SKID (Spline Kernel Interpolative Denmax)[1] to identify bound objects in our simulations. We have chosen to identify "clumps", which could be the progenitors to star clusters, as bound objects. SKID is able to identify groups of bound gas particles and so is perfect for this purpose.

4.1.1 Finding clump masses with Astrodendro

The package astrodendro uses dendrogram trees to identify related structures. Dendrograms are particularly useful for identifying objects embedded in larger hierarchical structures, in a way that requires limited parameter choices (Rosolowsky et al. 2008; Colombo et al. 2015).

In order to pass data through the astrodendro package we convert all of our data into synthetic FITS files. For this conversion we use the method of Ward et al. (2012), wherein particles are mapped into pixels and then smeared using

---

[1] https://github.com/N-BodyShop/skid

the the SPH smoothing kernel. To make the identification more straightforward we zoom in on a region surrounding the clump, with a width of 1 kpc. For this analysis we use pixel sizes of 10 pc. At this time we do not make any attempt to map the gas to CO emission, and instead use the surface density.

The only parameter we set in astrodendro is a minimum value required for a pixel to be considered part of the tree. We have experimented with other parameters (mindelta, minnpix), but find that at our resolution they make little difference. We experiment with two thresholds for the tree. The first is a surface density of 100 $M_\odot/pc^2$, above which we can estimate that star formation would proceed. This is close to the extinction threshold of Lada et al. (2010). The second is a surface density of 10 $M_\odot/pc^2$, above which gas transitions to being mostly molecular (Bigiel et al. 2008). We find that this threshold makes little difference to the masses of the objects found. From this point on, we use the higher threshold of 100 $M_\odot/pc^2$ to build the trees.

4.1.2 Finding clump masses with SKID

SKID is an Nbody group finder. It identifies structures using a friends-of-friends algorithm. Each structure then has unbound particles removed. Thus the final group contains only the bound mass formed. To find these masses with SKID the only essential parameter is a linking length. We choose a group linking length of 20 pc. Additionally, we consider only particles above 100 cm^{-3}, as these particles are dense enough to be part of the molecular medium. When recording the mass using SKID we take the mass of the central bound object. For the remainder of this section we report results using only SKID. We defer a detailed comparison of SKID and AstroDendro to a later section.

4.2 Clump masses in the turbulent disk

Figure 1 shows results for the cold, warm and hot disk. The right column of Figure 1 shows the mass histograms for bound objects in the disk, while the right panel shows surface density maps of the disks at the measurement time. The Toomre mass is plotted in each histogram panel as the dashed line. The maximum masses produced are 5.3×10^6 $M_\odot$, 1.1×10^8 $M_\odot$ and 2.5×10^8 $M_\odot$ for the cold, warm and hot disk, respectively.

The Toomre mass is sometimes proposed as the typical starting mass for clumps. If we compare our measured clump masses to the Toomre mass, we can see that there is a disagreement. Our measured maximum masses are consistently smaller than the Toomre mass, sometimes by an order of magnitude. While this is interesting in and of itself, using the full disks may introduce biases into measuring clump masses. For instance, laying turbulence everywhere introduces a competitive fragmentation scenario. Since the growth times for the smallest modes is shortest, the smallest size scales should collapse first. This competitive fragmentation may bias these disks to smaller clump masses. Further study is required to confirm that Toomre scale clumps are unlikely.

5 SEEDING CLUMP FORMATION

We now move on from the full turbulent disks discussed in the previous section. The fully turbulent disks have set an expectation for the range of clump masses possible in each of our quiet disk ICs. However, they are not a perfect comparison point. In particular, it is not possible to link each clump with the size scale and strength of the perturbation that seeded it. If we wish to compare to the Toomre mass, and the cases discussed in Section 2, we require a more controlled setup.

5.1 Seeding clump formation in quiet galaxies

In this section, we present a new approach to studying clump formation, or more generally the formation of bound structures, in simulations. In nature, turbulence is generated on large scales and then cascades down to feed smaller scales. It is these smaller scales which are of key interest in star formation. However, simulations struggle to capture the full turbulent cascade; it is difficult to resolve and maintain the full turbulent spectrum at the resolutions available for most galaxy-scale simulations (Kritsuk et al. 2007).

In Section 4, we avoided this problem by laying down a spectrum of turbulent velocities at the beginning of the simulation. The shape of our perturbation is modelled by the function

$$\Delta \vec{v} = -v_0 \left(\frac{r}{l/4}\right) e^{-0.5(r^2/(l/4)^2)} e^{0.5} \cdot \hat{r}, \tag{6}$$

where r is the distance from the centre of the perturbed region, v_0 is the chosen perturbation velocity, and l is the chosen perturbation wavelength. We choose this form such that $v_{max} = v_0$ at $r = l/4$, similar to a sine wave with wavelength l but quickly returning to zero. For this function, the divergence is almost uniform (and negative) for $r < l/4$ and then smoothly returns to zero. Thus the characteristic collapse time is $l/(4v_0)$.

Effectively, we are introducing a radially compressive mode in the region of interest, such as could be generated by local feedback events. By then choosing different combinations of disk mass, perturbation wavelength and perturbation velocity, we can build a large parameter space of cases. In this way we can explore the conditions that led to bound structure formation in disks of different masses.

5.2 Comparison of SKID and astrodendro

The clump masses as found by SKID and astrodendro agree when compared, after 30 Myr (the differences in the warm disk are no more than a factor of two). To illustrate this agreement, we choose two of our seeded clumps and follow their masses as a function of time with both SKID and astrodendro. The results of this analysis are shown in Figure 2. The left panel shows the results for a cold disk with a wavelength of 1 kpc and perturbation velocity of 10 km/s. The right panel shows the results for a warm disk with a wavelength of 1 kpc and a perturbation velocity of 30 km/s. The different coloured lines show different different clump finding methods; the purple line shows the results for SKID while the green line shows the results for astrodendro in
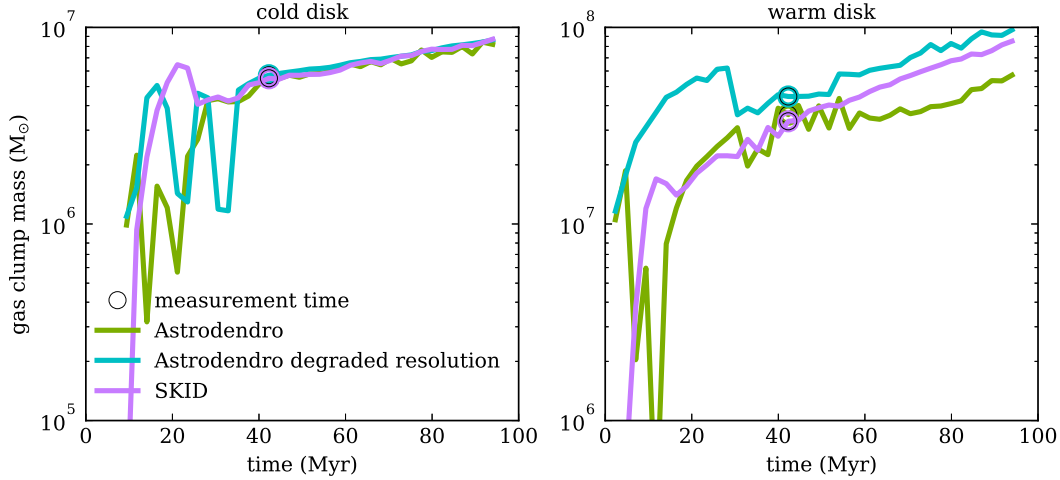
Figure 2. A comparison of the clump masses found by astrodendro versus SKID in the cold (left) and warm (right) disk. The green line shows the clump mass found by astrodendro as a function of time. The teal line shows the mass found by astrodendro if the initial resolution of the map is degraded to 100 pc. The purple line shows the bound mass identified by SKID as a function of time. The circles denote the time at which we record the mass measurement.

each panel. Additionally, the teal line shows the results for astrodendro with the resolution degraded from 10 pc to 100 pc.

There are significant differences in the identified masses, but these differences occur while the clumps are still forming. The important region to consider is the span of time after which an identifiable bound object is formed. As mentioned previously, we take our mass measurements after ~ 30 Myr, this time is denoted as an open circle in Figure 2. In the cold disk, after this time, there is less than 10% variation between the different methods. As noted above, there are slightly larger differences when looking at the warmer disk, where the background surface density is intrinsically higher.

5.3 Clump Evolution

As mentioned previously, for the purposes of analysis we define a "clump" as a bound gas structure. We further require that this structure formed as a result of one of our seeded perturbations. To identify cases that are able to grow structure, we track the surface density of the perturbed region. For each case, we track the surface density in a 50 pc apertures centred on the initially perturbed particles. A sample plot for the evolution of the surface density with time can be seen in Figure 3 for five cases. The cases in Figure 3 span a range of velocities, from 1 to 15 km/s, but the wavelength of the initial perturbation is held constant at 1 kpc. The evolutionary tracks separate themselves into two distinct sets, those that increase in surface density and those that do not; we will discuss this in depth in the following sections.

To help visualize what our clump evolution actually looks like, we have plotted sets of surface density maps in Figures 4 and 5. For Figure 5, the snapshots are taken at the shear time,

$$t_{\mathrm{shear}} = \frac{1}{\kappa}, \qquad (7)$$

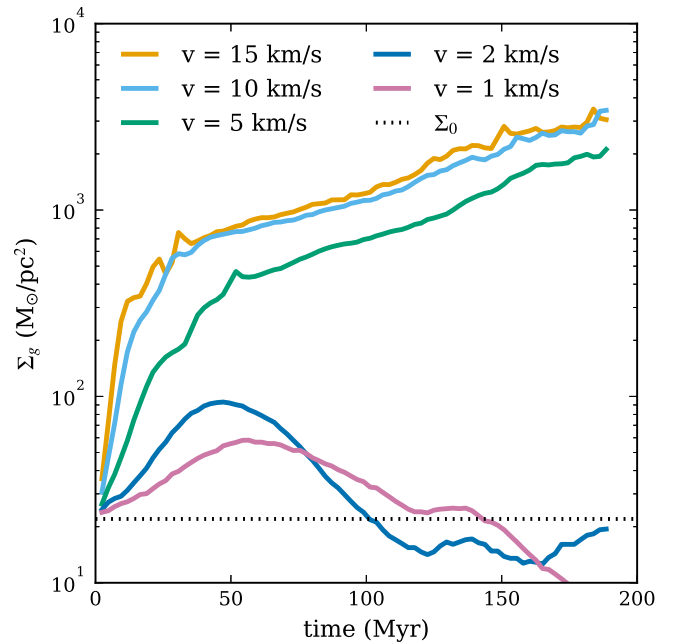where κ is the epicycle frequency for the disk. In this case

Figure 3. The evolution of the surface density for perturbations in the cold disk. The lines plot the surface density in a 50 pc aperture centred on the initially perturbed region. The cases with the smallest velocities, 1 and 2 km/s, show examples of perturbations that failed and could not produce a clump. The larger velocities, 5, 10 and 15 km/s, show examples of perturbations that produced a central clump.

the shear time is 15.5 Myr. This is the time to shear out a distance equal to your size.

We choose the shear time as the time to take representative snapshots as the perturbations have their fate determined by this point. On this timescale, a sheared structure can be shifted by order its own size; it is the period of a full epicycle. In this disk there are two main ways for
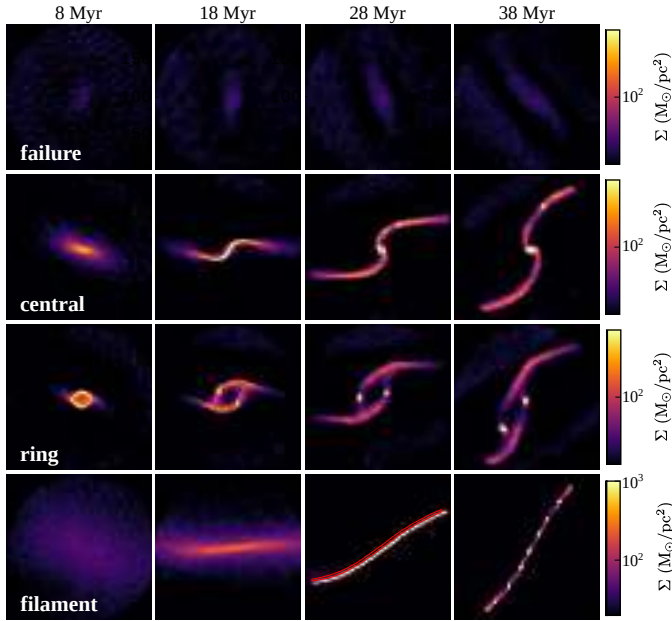
Figure 4. Evolution of the surface density for different clump formation scenarios over time. *Top row*: a failed clump, as discussed in Section 5.4. *Second row*: a central clump, as discussed in Section 5.5. *Third row*: two ring clumps, as discussed in Section 5.6. *Bottom row*: a filament, as discussed in Section 5.7.

a perturbation to fail. The first is thermal support due to the background sound speed in the disk. The second results from rotational support: this rotational support is associated with the initial shear and any later stretching due to ongoing shear. Thus, after one epicycle the perturbation should have started to collapse, or otherwise have begun to be sheared apart.

For the remainder of this section we discuss only the cold disk and use it as a case study to illustrate key concepts. All of the behaviour and cases discussed occur in all three of our galaxy disks, just in different regions of the $l - v$ parameter space.

5.4   Failed Perturbations

Referring back to Figure 3, two of the cases, with velocities of 1 and 2 km/s, are examples of perturbations that were not able to grow. Initially, they experience an increase in surface density, however, by ∼ 50 Myr, both have turned over and decrease until they oscillate around the background surface density of the disk; they are sheared apart. This behaviour can be seen in the top row of Figure 4, where a sample surface density map is shown, in time spacings of 10 Myr. After 38 Myr of evolution, right before we take a mass measurement, there is no dense structure present. Cases like these are deemed "failures" and, looking at Figure 5, they occur mainly in the low velocity range. We can further define these cases as those that experience a turnover in their surface density.

The bottom two rows in Figure 5 show examples of failed cases, which are outlined in red. In a direct analogy with the Toomre criterion for linear perturbations, clump collapse can be opposed by both shear and pressure. The rel-

evant timescales are the shear time and the sound-crossing time. Typically, depending on the scale, one of these dominates within a small region. Within a region roughly half the Toomre length, they are comparably important. This is quite similar to expectations for the linear, axisymmetric case (i.e. the Toomre criterion) and the non-axisymmetric case (Goldreich & Lynden-Bell 1965b). In both those scenarios, and in this work, it is always the case that pressure and rotation work together to dissipate structure. Moving away from axisymmetry slightly boosts the role of rotation (see eqn 5).

The failed cases in Figure 5 trace out a rough parabolic shape. This parabola is reminiscent of the growth rate as a function of *k* for the Toomre instability. In the pure axisymmetric case, rings cannot shear and so the shear time is not important. In that case, any growth rate larger than zero leads to the growth of structure. However, in our non-axisymmetric case, rings can shear. This means that the growth rate must compete with the shear time: if the growth rate is not sufficient, perturbations will be sheared apart before structure forms. In our study, this is the case for long wavelengths. For shorter wavelengths the competition comes down to the pressure, or the sound crossing time. At those wavelengths, the sound crossing time must be less than the collapse time. In the coldest disk, this effectively requires that the perturbation velocity be larger than 5 km/s.

5.5   Central Clumps

Cases where clumps have formed in the centre of the initially perturbed region are the easiest to interpret. They can easily be identified because the evolution of their surface density shows a rapid phase of increase, followed by a phase of constant, steady growth. In Figure 3 the cases with velocities of 5, 10 and 15 km/s are perfect examples of cases that form central clumps.

We note that at later times, when the surface density has climbed too high, these clumps are numerically poorly resolved. We know that they are bound and expected to collapse further. This has been shown analytically by (Goldreich & Lynden-Bell 1965b) for non-linear collapsed perturbations with an isothermal equation of state. However, the precise evolution of the surface density with time would require adaptive resolution beyond that employed here. For that reason, we do not place any special meaning on the steady exponential growth phase seen for collapsed objects past ∼ 50 Myr (as is seen in both surface density and mass, as shown in Figures 2 and 3).

We are also able to identify trends between the initial perturbation parameters and the resulting surface density of the central region. We see that as the initial velocity is increased, within a shear time, it is possible to get higher and higher surface densities. This effect does begin to saturate if the velocity gets too high, above ∼ 15 - 20 km/s (see next section).

The second row of Figure 4 shows an example of the evolution of a central clump. There is a stark difference when this case is compared to the surface density of the failed case. For a central clump, already by 8 Myr the surface density in the middle of the perturbed region has surpassed 100 $M_\odot/pc^2$ and by 28 Myr there is clearly a dense bound structure present. In Figure 5 these central collapse cases are
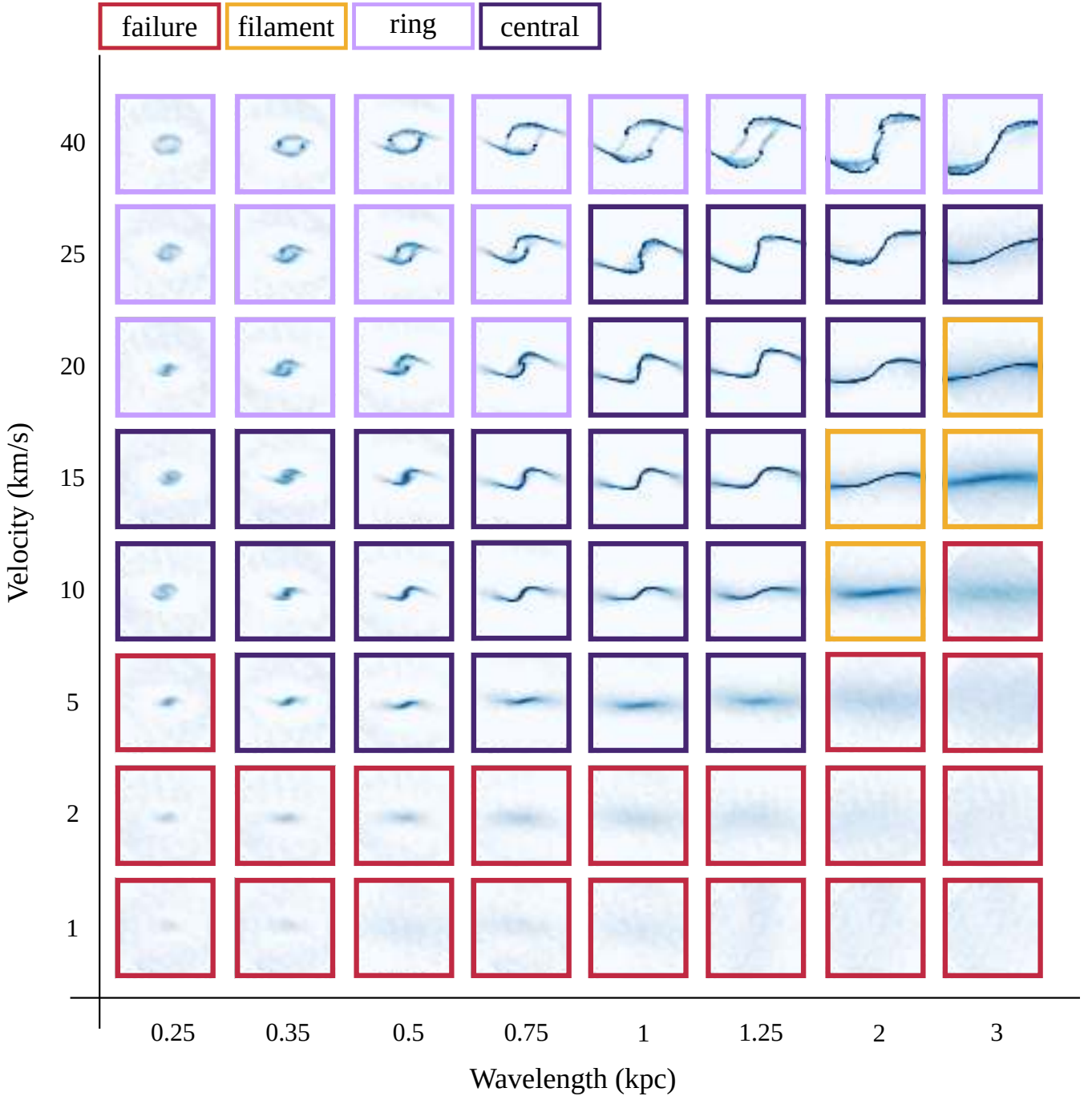
Figure 5. Sample surface density images of different perturbations in the cold disk. There are four different types of cases when considering the evolution of the perturbation. Weak perturbations, with low velocity are clear failures; these images are outlined in red. Successful cases are those that form a dense object at their centre, where the original perturbation was centred. These cases are outlined in dark purple and occupy a distinct region in the *l*-v space. Strong perturbations, with high velocity, often lead to the formation of ring clumps. These cases are outlined in light purple. Lastly, are cases we label as filamentary. These are cases that exceed the maximum mass per unit length of a filament for fragmentation. These cases are outlined in yellow. These snapshots are taken at the shear time for the disk, ~ 15.5 Myr, and are 1 kpc across.

deemed "centrals" and outlined in dark purple. They occupy a specific region of the $l - v$ space.

For this scenario of clump formation, in the cold disk, masses between 8.47×10^5 M$_\odot$ and 1.6×10^7 M$_\odot$ are possible. All the results for our measured clump masses are plotted

in Figure 7, where the top panel shows the cold disk we discuss in this section. Clumps that form by fragmenting in the centre of the perturbation, as discussed here, are plotted as filled symbols. In Figure 7 we can see general trends with both velocity and wavelength. Generally, as the velocity is

increased, the masses of the central clumps also increase. Similarly, as the wavelength of the perturbations is increased the masses of the clumps formed tend to increase as well.

5.6 Ring Clumps

A clump forming in the centre of a perturbation in the location where all of the velocities were directed is the most straightforward situation. However, there are more complicated scenarios that lead to the formation of bound structures. One such scenario involves the fission of a ring-like structure. The perturbations are initially directed radially inward. The higher the initial velocity, the larger the radius from which material can reach the centre quickly, within the shear time, for example. The angular momentum of the initial disk material with respect to the centre of the perturbation increases as r^2, where r is measured from the perturbation centre. Therefore, for large velocities the angular momentum per unit mass of the initially collapsed clump becomes quite high. This high angular momentum can cause the centre region to have too much rotational support and thus re-expand as a ring.

This ring expands and, as it does, is caught in the large-scale shear flow. This means that portions of the ring can be dragged spinwise or counter-spinwise until they are ultimately stretched out to join tidal-like features. The rings thus have strong m=2 type modes, which results in two over-densities rather than one.

The third row of Figure 4 shows an example of the evolution of two ring clumps. Here again by 8 Myr the surface density has exceeded 100 $M_\odot/pc^2$, this time in the ring structure. By 20 Myr, the two ring clumps have begun to fragment. By 38 Myr, the ring has begun to be sheared apart, and the two ring clumps are clearly visible. Fragmentation in high spin cases leading to multiple objects has been found to occur in protostellar disks (Kratter & Matzner 2006; Kratter et al. 2008).

Since this scenario requires a large angular momentum per unit mass in the centre of the perturbed regions, these cases are seen at high velocities. In Figure 5 the ring cases are outlined in light purple and can be found for cases with $v \gtrsim 20$ km/s. For the final masses in these cases we take the total bound mass of the two ring clumps.

The clumps formed from rings tend to have similar masses to central clumps when the two bound structures are counted together. In this case, total masses of between 9×10^5 $M_\odot$ and 1.8×10^7 $M_\odot$ are typical in the cold disk. When considered individually though, the clumps are less massive than those formed through the central fragmentation scenario. In Figure 7 the open symbols show the masses of ring clumps. Generally, these clumps follow the same trends as the central clumps. As the velocity is increased the clump mass increases, and as the wavelength is increased the clump mass increases. We can also see that, in general, the ring clumps have total masses that are higher than the central clumps. These high spin objects are consistent with the idea that observed large objects could be the result of beam crowding. In that case, we would actually be seeing the mass of multiple clumps in close proximity that formed out of a similar structure.

5.7 Filamentary Fragmentation

As noted earlier, when considering non-axisymmetric perturbations and long enough timescales, shear dominates the evolution of everything except the innermost bound clump. The shear will eventually draw the unbound material out into ever elongating tidal arm features. In an unrealistically quiet disk (such as in the controlled cases here) and over very long timescales, this material is wrapped to form a ring-like structure. In practice, the galaxy would have other perturbations acting on smaller timescales that break the the material up and use it to form other structures. However, there is an intermediate stage where the features are drawn out into filaments.

Perturbations with long wavelengths can exhibit a different mode of fragmentation. As time passes the long structures begin to behave like star-forming filaments. Such a filament will begin to fragment once it's mass exceed the critical line mass,

$$M_\text{line} = \frac{2c_s^2}{G} \tag{8}$$

where c_s is the sound speed and G is the gravitational constant (Inutsuka & Miyama 1997). For our coldest disk the line mass works out to 11,624 $M_\odot/pc$. The average width of our long wavelength filaments is on the order of 40 pc. This means that our filaments only have to exceed surface densities of ~290 $M_\odot/pc^2$ to be above the critical line mass and begin to fragment.

As time goes on and shear continues to operate, the filaments become more and more drawn out, decreasing the mass per unit length. This suggests there is a set time limit for the fragmentation in these objects to begin. If the original density of the filament is not high enough they will just be sheared apart.

We see this exact behaviour in many of our long wavelength perturbations. The bottom row of Figure 4 shows an example of a perturbation that develops filamentary behaviour and then fragments. By 18-28 Myr the density in the filament has begun to exceed the critical surface density calculated above. Indeed, by 38 Myr the filament has completely fragmented.

More examples of these filamentary cases can be seen on the right side of Figure 5, outlined in yellow. We label any structure produced by this phenomenon as secondary fragmentation. While it does lead to bound structures, there is different physics responsible for their production on top of our initial perturbation. In general these fragments are less massive than the central or ring clumps for comparable wavelengths and velocities. For example, at a wavelength of 2 kpc and a perturbation velocity of 10 km/s, the filamentary fragments are on average 2.4×10^6 $M_\odot$. As noted above, only very quiet disks would get the opportunity to use this mode of fragmentation so we have elected not to use it when comparing to observed disk properties. These masses are not included in Figure 7 or in any of the following discussion of mass.
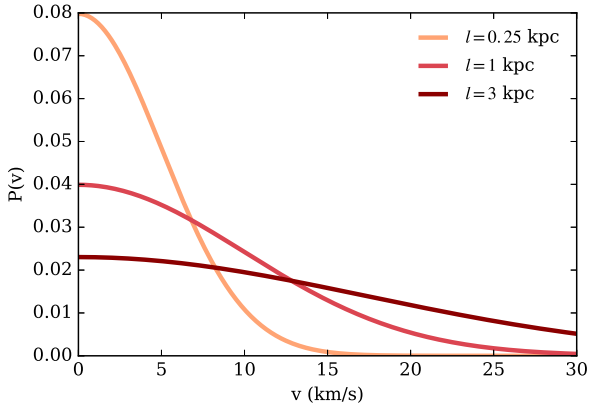
Figure 6. Sample probability distributions for three different wavelengths in the cold disk. These are generated assuming a spectrum of the form shown in equation 9. These are examples of the spectrums used to generate the most likely mass for each wavelength. As we can see from the plot, for the cold disk. velocities above 15 km/s are very unlikely.

6 WHAT IS THE MOST LIKELY CLUMP MASS?

In this section we use our measured clump masses to determine the most likely clump mass in a given galaxy. We begin with the coldest disk in our sample. In nature, bound structures, like clumps, are seeded by a cascade of turbulent energy. An extensive amount of work has been done to characterize the nature of this turbulence in molecular clouds (Myers 1983; Solomon et al. 1987; Kritsuk et al. 2013). There is a correlation between the velocity dispersion, or linewidth, and the size of a region (Larson 1981). Larson's first relation states

$$\sigma = A \, l^{1/2}, \tag{9}$$

where σ is the velocity dispersion, A is the normalization, and l is the scale at which that velocity is generated. For the cold disk, we assume that turbulence is generated by superbubbles, as it is in Milky Way-type galaxies. This gives $\sigma_0 = 10$ km/s, which is generated on a scale on the order of the scale height of the galaxy, $l_0 = 1$ kpc.

In order to assign a likelihood to each of our clump masses, we assign a probability to the velocity that seeded it. To assign this probability, we next assume that all of the velocities at a given wavelength are drawn from Gaussian distributions. Samples of the Gaussian distributions are shown in Figure 6 for three different wavelengths; 0.25, 1 and 3 kpc. Generating turbulent velocities by drawing from a Gaussian distribution is common practice (e.g. Price & Federrath 2010).

In general, coherent velocities on large scales above 10 km/s begin to get more and more unlikely. By convolving these probabilities with the clump mass distributions that result from each velocity we can determine the most likely mass at each wavelength. The results of this analysis are shown in the top panel of Figure 7. In the middle panel of Figure 7 we plot the mass distribution for the warm disk, and the hot disk in the bottom panel. For these cases we assume a velocity dispersion of $\sigma_0 = 50$ km/s (Wisnioski et al. 2015). For the generation scale, we assume that this

level of turbulence would be generated on a disk scale length, on the order of 3 kpc.

It is important to note that this study is useful for providing upper bounds on clump masses formed via fragmentation, since we do not include any star formation or feedback and do not account for any late stage accretion. That being said our approach offers a way to identify the most likely space for clump formation to operate in a given galaxy. In Figure 7 the dotted black line shows the most likely mass at each wavelength, while the grey shaded regions shows the 1σ probable region. We can see that in the cold disk, it is possible to get objects that begin to approach the predicted Toomre mass. However, the velocities required to form these objects are very high; they are not probable velocities. This in turn implies that while it is possible to make these larger bound structures approaching 10^7 M$_\odot$, it is not a likely outcome. This remains true as the disk mass, and thus the clump mass, is increased.

We can identify trends when considering the plots in Figure 7. First, as the velocity of the perturbations is increased, the mass of the resulting clumps increases. This is expected based on the the same trend observed for surface density in Figure 3. Second, there is a preferred mass scale for objects in a given disk. For the coldest disk the preferred fragmentation mass lies around 3×10^6 M$_\odot$, and little variation is seen away from this. This preferred mass lies around 4×10^7 M$_\odot$ and 5×10^8 M$_\odot$ for the warm and hot disks, respectively. As we increase the disk mass, of course, the clumps that form are generally more massive.

Additionally, there is a preferred fragmentation length in each disk. This length increases as the disk mass is increased. It is not possible to form bound structures below 0.25 kpc, 0.85 kpc, and 2 kpc for the cold, warm and hot disk, respectively. The physics behind these cutoffs was discussed in the previous section.

6.1 The Toomre Mass

As we did for the turbulent disk, we can compare the measured clump masses to the Toomre mass. As a reminder, for the coldest disk in our sample the critical wavelength is 940 pc, while the Toomre mass is 1.5×10^7 M$_\odot$. The Toomre mass is plotted as the orange star in Figure 7. The solid black line shows what the enclosed mass would be at different wavelengths. For the cold disk there is almost an order of mass discrepancy between the Toomre mass, and the expected mass (dotted line) at the critical wavelength. As the wavelength increases, so does the discrepancy between our measured masses and the ad hoc Toomre mass estimates.

In the warm disk, the critical wavelength is 2.4 kpc, which gives a Toomre mass of 2.9×10^8 M$_\odot$. If we move to the hot disk those get even larger, with a Toomre mass of 4.1×10^9 M$_\odot$ resulting from a critical wavelength of 5.4 kpc. These results are summarized in Table 1. Again, we see that masses predicted from Toomre theory are consistently over-estimates when compared to our seeded clump masses.

We find that our masses are between a quarter and half of the expected Toomre mass. While the Toomre prediction is linear in construction, as objects grow more dense and fragment their behaviour is increasingly non-linear. This is exacerbated by taking the results of a 1-d planar analysis, and translating it to a 2-d estimate of the mass. For these
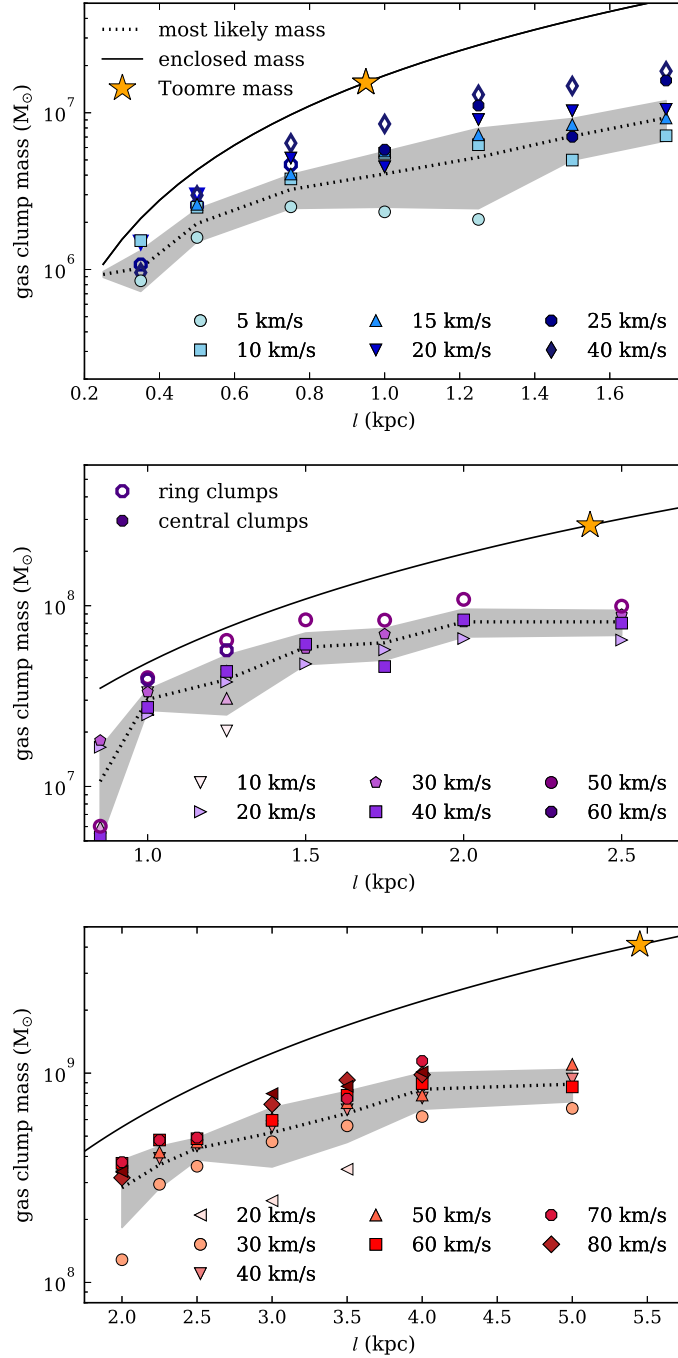
Figure 7. The most likely clump mass. *Top*: the masses in our cold disk. *Middle*: the masses in our warm disk. *Bottom*: the masses in our hot disk. In each plot the filled symbols denote central clumps, the open symbols denote ring clumps and the stars show the Toomre mass at each wavelength. The grey dashed line shows the mean expected mass and the shaded region shows the 1σ deviation (see section 6). Our measured clump masses wind up being smaller than the predicted Toomre mass. The shaded 1σ region also shows us that, while it is possible to get closer to the Toomre mass, it is not a likely case in nature.

reasons, it is not entirely clear if discrepancies result from the non-linear nature of fragmentation or the application of that theory to mass predictions. Secondly, the system, and few systems in nature, are axisymmetric. Finally, as the mass of the disk and its sound speed increase, the critical wavelength likewise increases. In our most massive, hottest, disk the critical wavelength increases to 5.4 kpc. A critical wavelength that large represents a significant portion of a galaxy disk. In fact, at high redshift, that may be the entire radius of the galactic disk. This has likewise been noted by Reina-Campos & Kruijssen (2017). Through angular momentum considerations alone this scenario is not possible: the collapse of the whole disk is ruled out and thus $l \gtrsim r_d$ must fail.
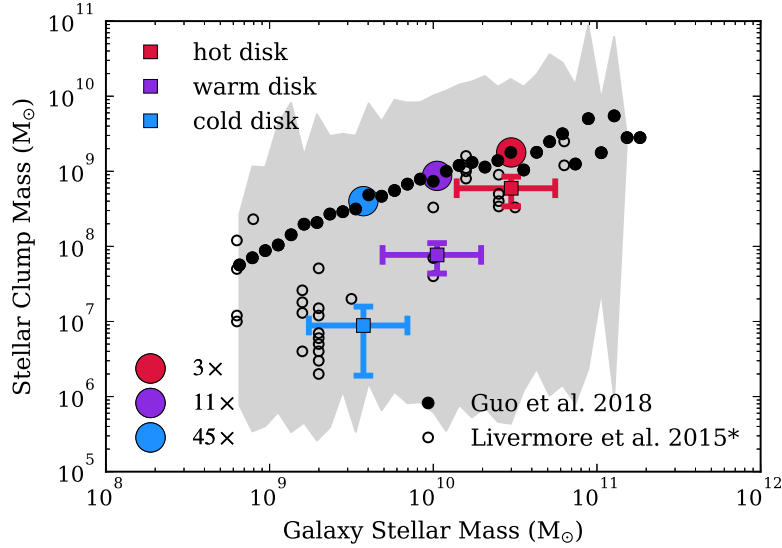
Figure 8. The expected clump stellar clump mass as a function of the stellar mass content of the galaxy. The average of our seeded disk clumps is plotted as each of the filled squares. The vertical errorbars show the standard deviation of the data. The horizontal errorbars show possible values of gas fractions for the conversion from gas to stellar galaxy mass. Two observational samples are plotted for comparison. The black circles shows the average clump mass in 0.5 dex mass bins for the sample of Guo et al. (2018) and the grey shaded region shows the range spanned by the data. The green circles show our estimate of the clump mass for the lensed sample detailed in Livermore et al. (2015). To convert from the original SFR measurements of Livermore et al. (2015) we assume that a clump's lifetime is 100 Myr, and that the measured SFR is sustained for this entire time. The large red, purple and blue filled circles show the level of beam crowding we would require to agree with the average CANDELS clump in a galaxy of comparable mass.

7 DISCUSSION & OBSERVATIONAL IMPLICATIONS

Up to this point we have assumed very fine resolution for our measurements. This makes our mass measurements most comparable to high resolution work, like that of Johnson et al. (2017b), with effective resolution of 40 pc. To compare to a broad range of observational results we must try to account for the possibility of coarser resolution.

We choose 1 kpc, to be comparable to the beams in the CANDELS survey which are typically between 500 pc to 1 kpc. This is in the range of resolution for multiple other high redshift surveys. To compare to the stellar mass of clumps, we also estimate the location of newly formed stars in our disks. We do not employ star formation and stellar feedback in these simulations. However, we can tag likely locations for star formation by identifying all gas that surpasses 116 $M_\odot/pc^2$; this is the threshold identified by Lada et al. (2010) for star formation. The simulations we use for comparison in this section are the seeded disks, discussed in section 5.

To estimate the impact of beam smearing we then change the way we assign masses to our seeded clumps. Up until this point, the masses quoted are the masses of a single bound structure at the centre of the perturbation or two bound objects in the case of a ring structure. In this section, we take all bound structures identified in the inner 1 kpc around the perturbation centre. The results of this analysis are plotted as the squares in Figure 8. These points show the average of the masses found in each disk. The error bars show the standard deviation, found using the velocity averaging method discussed in section 6.

We have had to make assumptions about the stellar mass content of our disks. We are using isolated galaxies in static potentials so our sample is not indicative of galaxies that have high stellar mass content. Typical gas fractions for galaxies above redshift 0.5 can fall anywhere between 0.2 and 0.8 (Morokuma-Matsui & Baba 2015). Here we take the definition that the gas fraction is

$$f_g = \frac{M_g}{M_g + M_*}, \tag{10}$$

where M_g and M_* are the total gas and star mass of the galaxy, respectively. Again, since our galaxies cannot capture the dynamics of those with a high stellar fraction, we take the maximum possible gas fraction for our galaxies to be 0.5.

For comparison in Figure 8 we plot the sample of clumps discussed in Guo et al. (2018). The averages of the clump masses in galaxy mass bins of width 0.5 dex are plotted as the black circles. The grey shaded region shows the range of the minimum and maximum clump mass in each bin. We also plot the higher resolution lensed clump sample discussed in Livermore et al. (2015). We note that the sample of Livermore et al. (2015) originally states only star formation rates for their clumps. We have converted these to rough masses by assuming the clumps form stars at this steady rate for their estimated lifetime.

The clump lifetime is still a debated topic. Some theories suggest that clumps migrate into the centre of galaxy disks, which suggests their lifetimes must be longer than 150 Myr (e.g. Shibuya et al. 2016). Other studies suggest a quick disruption due to strong feedback, giving a shorter lifetime of around 50 Myr (e.g. Krumholz & Dekel 2010; Oklopčić et al. 2017). We take a clump lifetime of 100 Myr to convert the sample. This value means our masses estimated from the

Livermore et al. (2015) sample will be an underestimate for the mass if the clump lifetime is long, and an overestimate if the lifetime is short in nature.

On the lower galaxy mass end, for our cold and warm disks, our sample agrees quite well with the findings of Livermore et al. (2015). For our most massive galaxy, the hot disk, our clump masses agree well with both the Guo et al. (2018) and Livermore et al. (2015) samples. As further comparison, the large blue, purple and red circles in Figure 8 show how many of our clumps would have to be crowded in a beam to get our mass to the average Guo et al. (2018) mass. For the cold, least massive disk, we would need to have 45 of our clumps in the beam. This number becomes more reasonable as we move to higher disk masses, 11 clumps in the warm disk and only 3 in the hot. These smaller factors agree well with the the resolution scaling factors discussed by Cava et al. (2018).

Our results suggest insights into clump formation, particularly in galaxies on the lower mass end (below 10^{10} M$_\odot$). We stress that the observationally measured mass of clumps is not necessarily the mass at which they formed. Our results suggest that beam crowding likely plays a role in the measurement of large clump masses in these smaller galaxies. Alternatively, clump mergers may play a role in building larger objects. Tamburello et al. (2015) also find that clump-clump mergers are required to build the largest objects. If clumps are long-lived, late-stage accretion can also build clump masses. On the higher disk mass end there are other ongoing effects that we do not discuss nor attempt to capture here. However, our results suggest that the largest observed clump masses likely result from the crowding or clustering of smaller objects into larger observational beams.

8 SUMMARY & CONCLUSIONS

In this work, we have introduced a new method for studying the formation of clumps, or bound structures, in galactic disks. We seed clump formation events in initially stable isothermal disks, without star formation or feedback. We design these conditions to be purposefully simple and thus offer maximum control. Our clump mass spectrums are not impacted by feedback recipe choices, providing a complementary approach to other recent work that employs a variety of feedback assumptions.

By seeding turbulent clump formation events, we are able to study the exact conditions under which different clump masses form. In general, we find that our largest clump masses can be over an order of magnitude smaller than the Toomre mass. Our results suggest smaller initial masses for clumps than reported in some observational studies. This is consistent with the idea that those studies have large beams that encompass many bound objects. We stress that when making this comparison, the clump observational mass may be different than the initial mass: just because an object is observed to be massive, does not mean it formed at that mass through gravitational fragmentation.

Our method provides a new way to approach the problem of studying clump formation in simulations; it offers a new way to compare to observations. The method can be completely tailored to specific galaxies. The only requirements is that the rotation curve and surface density distribution for the galaxy are known. Our method provides a promising new way to study the formation of these clumps in specific galaxies without the biases introduced by including different feedback methods.

REFERENCES

Agertz O., Teyssier R., Moore B., 2009, MNRAS, 397, L64
Agertz O., Romeo A. B., Grisdale K., 2015, MNRAS, 449, 2156
Bate M. R., Burkert A., 1997, MNRAS, 288, 1060
Behrendt M., Burkert A., Schartmann M., 2016, ApJ, 819, L2
Bigiel F., Leroy A., Walter F., Brinks E., de Blok W. J. G., Madore B., Thornley M. D., 2008, AJ, 136, 2846
Binney J., Tremaine S., 2008, Galactic Dynamics: Second Edition. Princeton University Press
Bournaud F., et al., 2014, ApJ, 780, 57
Cacciato M., Dekel A., Genel S., 2012, MNRAS, 421, 818
Cava A., Schaerer D., Richard J., Pérez-González P. G., Dessauges-Zavadsky M., Mayer L., Tamburello V., 2018, Nature Astronomy, 2, 76
Colombo D., et al., 2014, ApJ, 784, 3
Colombo D., Rosolowsky E., Ginsburg A., Duarte-Cabral A., Hughes A., 2015, MNRAS, 454, 2067
Dekel A., Sari R., Ceverino D., 2009, ApJ, 703, 785
Dessauges-Zavadsky M., Adamo A., 2018, MNRAS,
Dessauges-Zavadsky M., Schaerer D., Cava A., Mayer L., Tamburello V., 2017, ApJ, 836, L22
Elmegreen D. M., Elmegreen B. G., Ravindranath S., Coe D. A., 2007, ApJ, 658, 763
Fall S. M., Chandar R., 2012, ApJ, 752, 96
Fiacconi D., Mayer L., Madau P., Lupi A., Dotti M., Haardt F., 2017, MNRAS, 467, 4080
Fisher D. B., et al., 2017, MNRAS, 464, 491
Förster Schreiber N. M., et al., 2009, ApJ, 706, 1364
Fukui Y., Kawamura A., 2010, ARA&A, 48, 547
Genzel R., et al., 2011, ApJ, 733, 101
Goldreich P., Lynden-Bell D., 1965a, MNRAS, 130, 97
Goldreich P., Lynden-Bell D., 1965b, MNRAS, 130, 125
Guo Y., et al., 2015, ApJ, 800, 39
Guo Y., et al., 2018, ApJ, 853, 108
Hodge J. A., Carilli C. L., Walter F., de Blok W. J. G., Riechers D., Daddi E., Lentati L., 2012, ApJ, 760, 11
Hopkins P. F., 2012, MNRAS, 423, 2016

---

[2] https://dendrograms.readthedocs.io/en/stable/
[3] http://www.astropy.org

Hopkins P. F., Kereš D., Murray N., Quataert E., Hernquist L., 2012, MNRAS, 427, 968

Inoue S., Dekel A., Mandelker N., Ceverino D., Bournaud F., Primack J., 2016, MNRAS, 456, 2052

Inutsuka S.-i., Miyama S. M., 1997, ApJ, 480, 681

Jog C. J., 1992, ApJ, 390, 378

Johnson T. L., et al., 2017a, ApJ, 843, 78

Johnson T. L., et al., 2017b, ApJ, 843, L21

Kratter K. M., Matzner C. D., 2006, MNRAS, 373, 1563

Kratter K. M., Matzner C. D., Krumholz M. R., 2008, ApJ, 681, 375

Kritsuk A. G., Norman M. L., Padoan P., Wagner R., 2007, ApJ, 665, 416

Kritsuk A. G., Lee C. T., Norman M. L., 2013, MNRAS, 436, 3247

Kruijssen J. M. D., 2012, MNRAS, 426, 3008

Krumholz M. R., Dekel A., 2010, MNRAS, 406, 112

Lada C. J., Lombardi M., Alves J. F., 2010, ApJ, 724, 687

Larson R. B., 1981, MNRAS, 194, 809

Livermore R. C., et al., 2015, MNRAS, 450, 1812

Mandelker N., Dekel A., Ceverino D., Tweed D., Moody C. E., Primack J., 2014, MNRAS, 443, 3675

Mandelker N., Dekel A., Ceverino D., DeGraf C., Guo Y., Primack J., 2017, MNRAS, 464, 635

McKee C. F., Ostriker E. C., 2007, ARA&A, 45, 565

Morokuma-Matsui K., Baba J., 2015, MNRAS, 454, 3792

Murray N., Quataert E., Thompson T. A., 2010, ApJ, 709, 191

Myers P. C., 1983, ApJ, 270, 105

Oklopčić A., Hopkins P. F., Feldmann R., Kereš D., Faucher-Giguère C.-A., Murray N., 2017, MNRAS, 465, 952

Price D. J., Federrath C., 2010, MNRAS, 406, 1659

Reina-Campos M., Kruijssen J. M. D., 2017, MNRAS, 469, 1282

Rigby J. R., et al., 2017, ApJ, 843, 79

Robertson B. E., Kravtsov A. V., 2008, ApJ, 680, 1083

Romeo A. B., Wiegert J., 2011, MNRAS, 416, 1191

Romeo A. B., Burkert A., Agertz O., 2010, MNRAS, 407, 1223

Rosolowsky E. W., Pineda J. E., Kauffmann J., Goodman A. A., 2008, ApJ, 679, 1338

Shibuya T., Ouchi M., Kubo M., Harikane Y., 2016, ApJ, 821, 72

Solomon P. M., Rivolo A. R., Barrett J., Yahil A., 1987, ApJ, 319, 730

Swinbank A. M., et al., 2010, Nature, 464, 733

Swinbank A. M., et al., 2011, ApJ, 742, 11

Tacconi L. J., et al., 2010, Nature, 463, 781

Tamburello V., Mayer L., Shen S., Wadsley J., 2015, MNRAS, 453, 2490

Tamburello V., Rahmati A., Mayer L., Cava A., Dessauges-Zavadsky M., Schaerer D., 2017, MNRAS, 468, 4792

Toomre A., 1964, ApJ, 139, 1217

Truelove J. K., Klein R. I., McKee C. F., Holliman II J. H., Howell L. H., Greenough J. A., 1997, ApJ, 489, L179

Wadsley J. W., Stadel J., Quinn T., 2004, New Astron., 9, 137

Wadsley J. W., Keller B. W., Quinn T. R., 2017, MNRAS, 471, 2357

Ward R. L., Wadsley J., Sills A., Petitclerc N., 2012, ApJ, 756, 119

White H. A., et al., 2017, ApJ, 846, 35

Wilson C. D., Harris W. E., Longden R., Scoville N. Z., 2006, ApJ, 641, 763

Wisnioski E., et al., 2015, ApJ, 799, 209

This paper has been typeset from a TeX/LaTeX file prepared by the author.